# Impedance Spectroscopy for Emerging Photovoltaics

Published as part of The Journal of Physical Chemistry virtual special issue "Young Scientists".

Elizabeth von Hauff[*]

Department of Physics and Astronomy, VU Amsterdam, De Boelelaan 1081, 1081 HV Amsterdam, The Netherlands

ABSTRACT: Impedance spectroscopy has been widely applied over the last decades to study electrochemical systems and solid-state devices. However, performing impedance spectroscopy on emerging photovoltaics presents new challenges related to the unusual material properties and complex device architectures. This review provides an introduction to impedance spectroscopy for researchers in photovoltaics and closely related fields. The review begins with a list of practical guidelines for performing measurements and analyzing data. After this, the mathematical basics are reviewed, and an introduction to circuit elements is given. This is followed by tips for collecting reliable data and reducing artifacts in the frequency spectra. The review then surveys common approaches in the field for analyzing data, including performing equivalent circuit modeling, analysis of capacitance-frequency spectra, and carrier mobility measurements. The underlying assumptions of each analysis approach, as well as the advantages, limitations, and potential pitfalls are discussed.
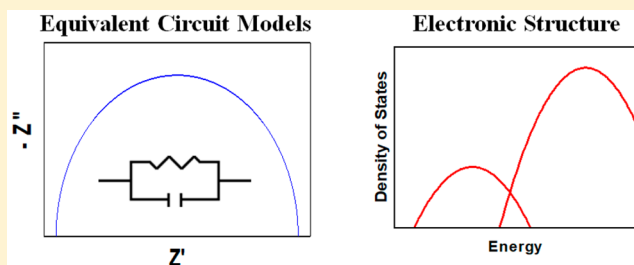
1. INTRODUCTION

1.1. Immittance Spectroscopy and the Permittivity Spectrum. Studying the interaction of electromagnetic fields with photo- and electro-active materials is at the heart of energy conversion research. The term immittance spectroscopy refers to a class of techniques, including impedance, admittance, capacitance, and dielectric spectroscopies, that are applied to gain insight into the physical and chemical properties of materials, interfaces, and multijunction devices, often as a function of applied voltage, illumination, temperature, or environmental stress conditions.

During an immittance measurement, the response of a sample to a time-varying electric field is monitored, and the fraction of electrical energy that is stored versus the fraction of energy dissipated by the sample, as well as the relaxation time scale (the time that it takes the sample to return to equilibrium after excitation by the input), is measured as a function of frequency. To ensure a linear response from the sample, the amplitude of the input signal is small. In other words, the sample is perturbed during the measurement but not irreversibly changed. In impedance and admittance spectroscopy, the input signal is an alternating voltage V_{ac} and relaxation processes, such as lattice distortions, electrode polarization, dipole rearrangement, and electrical and ionic conduction, are sequentially probed by varying the frequency of V_{ac} and measuring the alternating current response I_{ac}.

Immittance spectroscopies ultimately probe the permittivity ε of the sample. Figure 1 shows examples of the range of time scales, and the corresponding frequencies, of common relaxation processes in semiconductors and electrochemical cells. At very fast time scales (e.g., femtoseconds) changes in the permittivity spectrum due to electronic transitions can be studied with

Figure 1. Relaxation processes in semiconductors and electrochemical systems. The typical time scales are indicated in the top axis, while the corresponding frequencies are indicated in the lower axis. The arrows indicate the range of time scales for each process.

transient optical spectroscopy. At slower time scales (nanoseconds), molecular or lattice polarization, as well as dipolar rearrangement, may be observed with dielectric spectroscopy. Electronic and ionic conduction can be investigated with electrical spectroscopy at slower time scales (microseconds and slower). These relaxation events result in a frequency-dependent permittivity spectrum. Permittivity is a material parameter that depends on temperature and frequency of the time-varying electric field but not on the electric field strength. In the static case, the permittivity reduces to the dielectric constant. An ideal

dielectric (stores electrical energy) has a frequency-independent permittivity, while the permittivity of an ideal conductor (dissipates electrical energy) drops linearly with increasing frequency. The permittivity spectra of semiconductors and electrochemical cells contain frequency-dependent features reflecting processes such as electrical and ionic transport and dipole alignment.

Theoretically, varying the frequency of the input signal over an infinite range would make it possible to probe all possible relaxation processes in a sample with a single measurement. Technically and practically, however, experimental equipment for performing immittance measurements is limited to smaller frequency ranges. The term immittance spectroscopy was originally coined to describe electrical spectroscopy (impedance and admittance), which is performed between subhertz and megahertz and is used to study the resistive and capacitive properties of solid-state devices and electrochemical cells. Electrical immittance spectroscopy is useful to study electrical and ionic conduction, and "slow" (microseconds to seconds) charge transfer processes at material interfaces. The term dielectric spectroscopy generally refers to higher frequency measurements, megahertz to gigahertz, applied to probe the structural properties of materials, usually dielectrics. Terahertz spectroscopy is an optical spectroscopic technique that applies ultrafast optical signals to probe relaxation processes in the terahertz range and is not historically included in the class of immittance spectroscopies; however, the approach is analogous.

The broad application of immittance spectroscopy in physics, chemistry, material science, and engineering makes it difficult to summarize this topic concisely for a general audience. Interested readers are referred to books on the basics of impedance spectroscopy[1,2] as well as dielectric theory.[3,4] This review focuses on the application of electrical immittance techniques (impedance spectroscopy) to emerging photovoltaic (PV) materials and devices, such as dye sensitized solar cells (DSSC),[5] organic photovoltaics (OPV),[6] and perovskite photovoltaics.[7] Most of the examples for analyzing impedance spectra are based on results from OPV. This is, on one hand, because much work has been done in this field over the last decades, resulting in reliable frameworks for data analysis. On the other hand, OPV devices provide an interesting case study to connect concepts in electrochemistry and solid-state physics to develop tools and approaches for data analysis. Researchers in related areas, such as inorganic thin film photovoltaics, electrochemical energy conversion and storage, and emerging electronics may also find the concepts useful. Rather than a comprehensive survey of results from the literature, the aim is to provide a detailed introduction for newcomers on how to perform reliable impedance measurements, strategies for analyzing and interpreting the data, and potential challenges and pitfalls when impedance spectroscopy is applied to study new solar cell materials and device architectures.

1.2. Practical Guidelines for Performing Impedance Spectroscopy and Analyzing Data.
Here some practical guidelines, as well as potential pitfalls, are given to help to guide experimental design and data analysis, as well as to direct the more selective reader to relevant content in this manuscript.

1.2.1. Experimental Design. Impedance spectroscopy is a powerful diagnostic tool for the in situ monitoring of transport and recombination processes at different points along the solar cell current−voltage (*IV*) curve, investigating device aging and performance loss as the result of external stress factors, as well as identifying how variations in fabrication protocols influence solar cell parameters. However, a single impedance spectrum generally will yield no useful information. Therefore, to obtain useful insights, it is best practice to perform impedance spectroscopy as a function of an experimental parameter of interest, such as dc voltage, illumination conditions, temperature, the thickness of the solar cell active layer or transport layers, variation of contact materials, or as a tool to diagnose performance loss during aging tests. This will facilitate the interpretation of the spectra, and extraction of relevant physical parameters from the data.

1.2.2. Data Integrity. A prerequisite for the reliable analysis of impedance spectra is to ensure that there are no artifacts in the spectrum. This is not always an obvious or nontrivial task, as the source of artifacts ranges and also depends on the specific measurement setup, dc offset, illumination conditions, and the sample. The most common artifacts are due to a nonlinear sample response, inductance from long cables, irreversible changes to the sample during the measurement, and noise. Good practice is to check the compliance of the impedance spectra to the Kramers−Kronig relations (section 4.5 and section 5.1) for each measurement, and if necessary, modify the measurement procedure to remove any external sources of error.

1.2.3. Data Analysis. The most widely applied approaches to analyze impedance data from solar cells are equivalent circuit modeling and capacitance−frequency modeling. Equivalent circuit modeling (section 5) is a relatively quick strategy to describe the global sample response by quantifying the resistive and capacitive contributions to the impedance spectrum over the full frequency range of the measurement. To yield meaningful results, however, the circuit model must be based on the underlying physical parameters of the device. In the photovoltaic community, equivalent circuit models have been developed to describe the physical processes of carrier diffusion and recombination in the illuminated device. In these models, transport and recombination are considered as two independent relaxation processes occurring on distinct time scales, and carrier recombination is assumed to be a first-order, nonreversible reaction. This approach requires that both relaxation processes occur on time scales within the frequency window of the impedance measurement, i.e., microseconds (megahertz) to seconds (hertz). This is the case for electrochemical DSSC devices that are characterized by long carrier lifetimes (microseconds to milliseconds)[8−12] and OPV devices based on organic semiconductors with low carrier mobilities (10^{-7} to 1 $(V\,s)/cm^{-2}$),[6,13,14] as transport and recombination processes are sufficiently slow that they can be observed with an impedance measurement and therefore modeled with an equivalent circuit.

In the case of thin film PV, e.g., inorganic crystalline materials such as CI(G)s, CdTe, perovskites, electrical transport, and recombination processes are generally too fast to be accessed with impedance spectroscopy. In this case, the conductive contribution of free charge to the impedance spectrum is ignored, and the capacitance versus frequency (Cf) spectra (section 6) is used to extract parameters about electronic structure of the sample. For example, the Mott−Schottky analysis can be used to extract the doping profile and density, as well as the built-in voltage (section 6.1). This analysis requires a passive semiconductor−metal junction that is depleted of mobile charge, resulting in device capacitance that is frequency-independent over a well-defined range of the Cf spectrum. Cf spectroscopy can also be used to determine electronic trap profiles in the absence of mobile charge (section

6.2). The dielectric constant of the absorber layer can also be extracted from the Cf spectrum at low frequencies (section 6.3), provided the capacitance of the semiconductor can be extracted reliably and there is no contribution from mobile charge. Extracting reliable results with Cf approaches requires a well-defined depletion region in the device, which presents a serious challenge in the study of emerging PV devices, due to the presence of mobile charge and ions in the device, resulting in the violation of the depletion approximation and artifacts in the Cf spectrum. For example, metal−halide perovskite solar cells have been widely reported to show mixed electrical and ionic conduction,[15] and the contribution of mobile ionic species results in anomalies in the low frequency regime of the Cf spectrum. In the case of low mobility, intrinsic semiconductors, Cf spectra often show artifacts in the high frequency regime due to chemical capacitance and carrier freeze-out. Care must be taken to identify and interpret, or in the best case eliminate, the signatures of mobile ions and charge carriers in the Cf spectra as they can falsify the extracted parameters, e.g., built-in field, trap profiles, and dielectric constant.

To circumvent these challenges, impedance spectroscopy may serve as a useful tool for more specialized and fundamental studies of ion and charge transport. For example, ionic transport results in a clear signature in the impedance data that can be modeled with well-known circuit models. Furthermore, impedance spectroscopy can be applied to quantify carrier mobility values and identify signatures dispersive transport (section 7) in disordered semiconductors.

Table 1 summarizes the analysis procedures that are discussed in this review, along with the parameters that can be extracted, the assumptions and requirements for the analysis, the potential pitfalls of each approach when applied to emerging PV devices, and useful extensions to the measurement to facilitate reliable data analysis.

1.2.4. Corroborate Results with Independent Measurements. Corroborating the results obtained from impedance spectra with other measurements is good practice, especially if the interpretation of the spectra is ambiguous.

2. BASICS OF IMPEDANCE SPECTROSCOPY

2.1. Transfer Function and the Frequency Domain. Impedance spectroscopy is performed by applying an alternating voltage V_{ac} to a sample and measuring the current response I_{ac}. In the time domain (Figure 2a), V_{ac} and I_{ac} are sinusoidal functions that can be expressed as

$$V(t) = V_o \sin(\omega t) = V_o e^{i\omega t}$$

$$I(t) = I_o \sin(\omega t + \phi) = I_o e^{i(\omega t + \phi)} \tag{1}$$

where V_o and I_o are the amplitude of the voltage and current signals, respectively, ω is the angular frequency ($\omega = 2\pi f$), ϕ is the time delay between $V(t)$ and $I(t)$, and t is time. The impedance $Z(t)$ is given by

$$Z(t) = \frac{V(t)}{I(t)} = Z_o e^{-i\phi} \tag{2}$$

where $Z_o = \frac{V_o}{I_o}$.

Z is a transfer function, i.e., a function that relates the sample output (I_{ac}) to the input (V_{ac}) as a function frequency. Physically, the impedance is the complex (time-varying or frequency-dependent) resistance of the sample.

Table 1. Summary of Analysis Approaches Discussed in This Review, Parameters That Can Be Extracted with These Analyses, Assumptions and Requirements for the Analysis, Useful Extensions to the Measurement Protocol To Support Data Interpretation, and Potential Pitfalls When Each Approach Is Applied to Emerging PV Devices

| analysis	parameters that can be extracted	assumptions and requirements	useful extensions to facilitate data analysis	potential pitfalls
equivalent circuit modeling	global device response, relaxation time scales	physical motivation for circuit model; relevant transport processes slow enough to be observed with impedance spectroscopy	variation of absorber layer thickness, contact materials, dc offset, and illumination conditions	lack of unique correlation between circuit model and frequency response
capacitance-frequency modeling	doping concentrations, built-in potential, profile of trap states, dielectric constant	depletion approximation satisfied	temperature-dependent measurements to obtain activation energies of trap states	contribution to spectrum from carrier freeze-out, chemical capacitance, mobile ions, electrode polarization
transport studies	carrier and ion transport properties, insight into dispersive transport	transport slow enough to be observed with impedance spectroscopy	temperature-dependent measurements; different dc offsets	challenge to develop and apply transport models
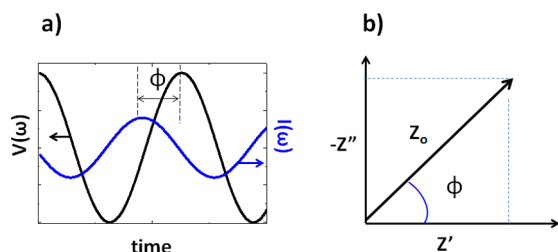
Figure 2. (a) Time-domain representation of $V(t)$ and $I(t)$. The phase angle φ depicts the time delay between the voltage input and the current response. (b) Frequency-domain representation of Z, including $Z_o = \frac{V_o}{I_o}$ and phase angle φ.

While the time domain is more intuitive, there are many advantages to representing dielectric functions in the frequency domain. Figure 2b shows the frequency-domain representation of Z. All the information contained in Figure 2a can now be concisely summarized in two quantities, namely, the magnitude Z_o and the phase angle ϕ. Varying the frequency of the voltage input results in a spectrum of Z values in the frequency domain.

In the complex plane, Z is expressed as

$$Z = Z' - iZ'' \tag{3}$$

where Z' is the real component of Z ($\phi = 0$), Z'' is the imaginary component of Z ($\phi = 90°$), and the magnitude of Z is given by $Z = \sqrt{Z'^2 + Z''^2}$. Physically, Z' is the resistance R, defined by Ohm's law as the resistance of a sample to current flow. Z'' is the reactance, sometimes denoted as X, and describes the resistance of the sample to changes in current flow.

$$Z' = R = Z_o \cos(-\phi) = Z_o \cos(\phi)$$

$$Z'' = X = Z_o \sin(-\phi) = -Z_o \sin(\phi) \tag{4}$$

Note that there are some differences in notation between different communities. For example, in physics it is customary to express Z'' as a negative quantity (due to the negative sign in eq 2 and eq 4), while in engineering it is more customary to express Z'' as a positive quantity.

The notation introduced here extends to all of the complex dielectric parameters. Table 2 shows the relationship between the dielectric parameters,[2] where Y is the admittance, ε is the permittivity, M is the dielectric modulus, and $\tilde{C}$ is the complex capacitance. Here, C_o is the capacitance of the empty cell ($C_o = \varepsilon_o A/d$, where A is the cell area, d is the thickness, and ε_o is the permittivity of free space) and $\alpha = i\omega C_o$.

Generally, representing the data in terms of Z, Y, and M is relevant for studying the conduction mechanisms of mobile charge, while representing the data in terms of ε and $\tilde{C}$ is more relevant for studying electronic structure and dielectric properties.

2.2. Basic Circuit Elements. The impedance can be represented in terms of ideal electrical circuit elements. Resistors

are dissipative elements that resist the flow of current. The impedance of a resistor is purely real ($\phi = 0$) and frequency-independent. An ideal capacitor C, in contrast, stores electrical energy. The impedance of a capacitor is purely imaginary ($\phi = 90°$) and varies inversely with frequency. An ideal inductor L stores energy in a magnetic field ($\phi = -90°$) by opposing changes in current flow via an electromagnetic force (EMF). The impedance of L varies proportionally with frequency. The circuit elements are summarized in Table 3.

Table 3. Impedances of Ideal Circuit Elements Resistor R, Capacitor C, and Inductor L

Element	Unit	Symbol	Z
Resistor R	Ω		$Z_R = R$
Capacitor C	F		$Z_C = \dfrac{1}{i\omega C}$
Inductor L	H		$Z_L = i\omega L$

2.3. Single Time Scale Relaxation: The RC Circuit. Ideal relaxation processes can be modeled using a circuit consisting of a resistor and capacitor in parallel, i.e., an RC circuit (inset Figure 3a). From Kirchhoff's current law,

$$0 = I_R + I_C = \frac{V}{R} + C \frac{dV}{dt} \tag{5}$$

Solving this differential equation for the voltage V yields

$$V(t) = V_o \exp\left(-\frac{t}{RC}\right) \tag{6}$$

where V_o is the voltage at $t = 0$. The time $t = RC$ is the characteristic time constant of the RC circuit. In electronics, this corresponds to the charging/discharging time of the capacitor in the circuit. For impedance measurements on physical systems, the time constant of the RC element is determined by the time scale of the dielectric relaxation.

The impedance of an RC circuit is given by

$$Z_{RC} = \frac{R}{1 + i\omega RC} \tag{7}$$

In the low frequency limit $Z_{RC} \approx R$. In the high frequency limit $Z_{RC} \approx \frac{1}{i\omega C} = Z_C$.

Figure 3 shows the impedance spectrum of an RC element. The representation of the impedance spectrum in the complex plane (Figure 3a) is commonly referred to as a Nyquist plot. An RC circuit results in a spectrum in the shape of a semicircle; this is easily seen by expressing eq 7 in terms of the individual real and imaginary components of Z_{RC} (see eq 3). The maximum of the semicircle is given by $\omega_p \tau = 1$, where $\omega_p = 2\pi f_p$ is the peak frequency, and τ is the RC time constant, i.e., the relaxation time

Table 2. Relationship between Dielectric Parameters[2]

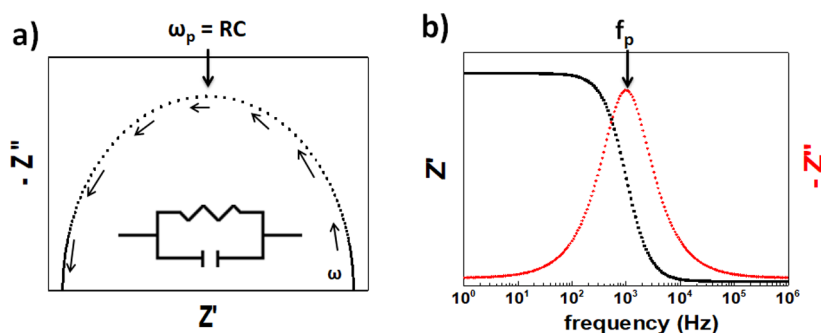| quantity	unit	Z	Y	ε	M	C
impedance Z	Ω	Z	Y^{-1}	$(\alpha Z)^{-1}$	$\alpha^{-1}M$	$(i\omega \tilde{C})^{-1}$
admittance Y	S	Z^{-1}	Y	$\alpha\varepsilon$	αM^{-1}	$i\omega\tilde{C}$
permittivity ε	F/m	$(\alpha Z)^{-1}$	$\alpha^{-1}Y$	ε	M^{-1}	$C_o\tilde{C}$
dielectric modulus M	m/F	αZ	αY^{-1}	ε^{-1}	M	$C_o\tilde{C}^{-1}$
complex capacitance C	F	$(i\omega Z)^{-1}$	$(i\omega)^{-1}Y$	$C_o\varepsilon$	$C_o M^{-1}$	$\tilde{C}$

Figure 3. (a) Nyquist plot and (b) Bode plot of the impedance spectrum of an RC circuit. A diagram of the RC circuit is shown as in inset in the Nyquist plot. The arrows indicate that the frequency increases toward the origin of the plot. In the Bode plot, Z' and Z'' versus frequency are plotted. The peak frequency $\omega_p = 2\pi f = RC$ is indicated in both figures.

scale. If the relaxation time scales are distinct, then the number of semicircles in the Nyquist plot of real samples gives an indication of the number of relaxation processes in the spectrum. If the relaxation time scales are similar, then the semicircles will overlap, and it may be necessary to model the data to distinguish relaxation processes. The Nyquist plot is most commonly used when equivalent circuit modeling is applied to analyze the data. The disadvantage of this visualization is that the frequency corresponding to each Z value cannot be extracted from the plot. Note that the frequency increases toward the origin of the graph, as indicated by the arrows.

The Bode plot (Figure 3b) is used to represent the frequency-dependence of dielectric parameters. The Z' versus frequency and Z'' versus frequency spectra for the RC circuit are represented in the same graph. The peak frequency in the $-Z''$ vs frequency spectrum (and change in slope in the Z' vs frequency) corresponds to f_p.

The RC circuit is a fundamental building block for modeling the impedance data from physical samples. It is characterized by a single time constant τ. Real samples, however, often demonstrate relaxations with a distribution of time constants.

2.4. Distributed Time Scale Relaxation: Nonideal Circuit Elements. The impedance response of the semi-infinite diffusion of particles at low frequencies, such as ions, i.e., mass transport, cannot be described with a simple RC element. The Warburg impedance Z_W is given by[16]

$$Z_W = \frac{A_W}{\sqrt{i\omega}} = \frac{A_W}{\sqrt{2\omega}} - i\frac{A_W}{\sqrt{2\omega}} \qquad (8)$$

where A_w is the Warburg coefficient and is given by the ac diffusion coefficient of the particles. The Warburg element yields a characteristic trend in the Nyquist plot, namely, a linear increase in Z values at low frequencies, with $\phi = 45°$.

The constant phase element CPE is a generalization of the Warburg element, and the impedance of the CPE, Z_{CPE}, is given by[1]

$$Z_{CPE} = \frac{1}{Q(i\omega)^n} \qquad (9)$$

where n is a dispersion parameter that determines the physical meaning of Q. If $n = 1$, the CPE reduces to an ideal capacitor and $Q = C$. If $n = 0$, the CPE reduces to a real resistor, and $Q = 1/R$. If $n = 0.5$, the CPE reduces to a Warburg element, and $Q = 1/A_w$. While the description of the CPE may appear arbitrary, this element is often used to describe relaxation processes with a distribution of time scales (i.e., time-dependent or dispersive processes), such as charge transfer at a nonhomogeneous

electrode surface,[1] or carrier transport in amorphous semi-conductors.[17,18] In this case, the ideal capacitor is substituted by a CPE element with $Q = C$ and $n > 0.5$ in the circuit. The distribution in relaxation times $(0.5 < n < 1)$ results in a "depressed" or distorted semicircle in the Nyquist plot.

3. PERFORMING IMPEDANCE MEASUREMENTS: PRACTICAL TIPS

Impedance spectroscopy is a relatively simple measurement to perform. However, for newcomers to the field it may be challenging to choose the right equipment, prepare the setup to measure samples, choose appropriate measurement parameters, and finally analyze the data. When it comes to equipment, there is a wide selection of commercial setups available depending on the samples you want to investigate. A quick checklist to guide that selection is

- Solid-state or electrochemical samples?
- two- or four-point measurement, or three-electrode measurement?
- Which frequency window is required?
- What current range and sensitivity are required?
- What range of voltage values (dc) is required?

Electrochemical impedance spectroscopy is commonly performed in a three-electrode geometry while solid-state solar cells are more commonly investigated in either a two-point or four-point geometry. The required frequency window is determined by the time scales of the relaxation processes that will be investigated. The range of current detection will be determined by the geometry and conductivity of the sample. The voltage range will depend on which dc offsets will be applied, e.g., which operating points on the IV curve will be investigated. Electrochemical impedance spectroscopy is done in the frequency range megahertz (microsecond) to subhertz (less than seconds), and most impedance spectroscopy performed on thin film PV is in this range as well. Measuring at lower or higher frequencies is possible but often presents technical challenges to acquire reliable data. At low frequencies, the measurement is time-intensive and susceptible to noise. At high frequencies, inductive effects from the setup, usually cables, can lead to artifacts in the spectrum that are not related to the sample itself.[19]

Most commercial providers of impedance analyzers provide demonstrations for performing measurements and analyzing the data. Commercial equipment comes with accompanying software for entering measurement parameters, performing data analysis, and exporting the data in the desired format.

11333

The impedance measurement is performed by applying a small signal alternating voltage (V_{ac}) across the sample and measuring the alternating current response (I_{ac}). The V_{ac} signal may be superimposed on a dc voltage offset to probe different points along the IV curve of the device. For a constant dc offset, the frequency of the V_{ac} input is varied, and I_{ac} is measured at each frequency, yielding the transfer function Z. Other dielectric parameters can be calculated from the impedance data (see Table 2). The user enters the value of the dc voltage offset, the amplitude of the driving voltage V_{ac}, the frequency range for measurement, including starting and end value and number of measurement points, and distribution of measurement points over the frequency range (usually in decades), as well as other parameters such as current range and integration time of the measurements, and the format of the output data.

4. CRITERIA FOR PERFORMING RELIABLE MEASUREMENTS: LINEARITY, CAUSALITY, STABILITY AND FINITENESS

The general prerequisite for obtaining reliable impedance spectra is that the measured transfer function Z satisfies the criteria of linearity, causality, stability, finiteness.[1]

4.1. Linearity. In circuit theory, linearity means that the input of the circuit is directly proportional to its output, in other words, the circuit demonstrates additivity (i.e., if $V_1 = I_1 R$ and $V_2 = I_2 R$, then $V_1 + V_2 = (I_1 + I_2)R$) and homogeneity (i.e., $V = IR$ and $kV = kIR$, where k is a constant).

The criterion for linearity is obviously not satisfied over the entire IV characteristic of a solar cell, or any energy storage or conversion device for that matter, as current generally varies nonlinearly with applied voltage. Therefore, to obtain a linear transfer function for Z, the amplitude of V_{ac} is chosen infinitesimally small so that the amplitude of I_{ac} varies pseudolinearly with the amplitude of V_{ac}. In the linear or pseudolinear limit, the impedance spectrum is independent of the amplitude of V_{ac}. This means small changes to the amplitude of V_{ac} result in linear changes in the amplitude of I_{ac} but no change in the value of Z. A rule-of-thumb is to choose the smallest possible amplitude for V_{ac} to avoid nonlinear artifacts in the Z spectrum. However, poor signal-to-noise can become a practical limit in this case. One quick and qualitative check for establishing a suitable V_{ac} amplitude is to zoom into the IV characteristics at the operational point of interest (ensure that there are enough measurement points available) and identify a measurement range in which current varies linearly with applied voltage. The pseudolinearity can be tested by varying the V_{ac} amplitude slightly about the chosen value, and ensuring that the Z spectrum does not change. A more rigorous check is to use Lissajous figures, or check that the data satisfy the Kramers–Kronig relations (section 4.5). The tolerable voltage range for pseudolinearity will depend on the measurement conditions, such as the applied dc offset voltage, illumination conditions, as well as the sample itself. In some cases, the linearity of the system may also be frequency-dependent. In this case, different amplitudes of V_{ac} can be used to acquire different frequency ranges of the spectrum, to ensure linearity over a smaller frequency range. The full spectrum is then stitched together from the individual spectra.

Performing impedance measurements in the nonlinear regime will result in higher harmonics in the frequency spectra, i.e., integer multiples of the input frequency in the current response. Some researchers have exploited this effect in the field of nonlinear impedance spectroscopy.[20] Nonlinear impedance spec-

troscopy is useful for studying nonlinear effects, increasing signal-to-noise, and widening the frequency range of the measurement. Commonly used approaches for analyzing impedance data (e.g., circuit modeling) rely on linearity; for this reason, the application and analysis of nonlinear impedance spectroscopy are beyond the scope of the current review.

4.2. Causality. In circuit theory, causality means that the system responds only to the V_{ac} input and not to external factors. For real samples, measurements that do not satisfy causality contain artifacts. Identifying and eliminating measurement artifacts in impedance spectra is challenging, as these may introduce frequency-dependent features that overlap with real relaxation processes. Common artifacts in the high frequency range are cable inductance and possible clipping of the V_{ac} amplitude, leading to distortions in the signal, due to instrumentation limitations. High frequency artifacts can be reduced by using short cables, performing reference measurements to determine the signatures from the measurement setup, examining the raw time-domain data to ensure that the V_{ac} signal amplitude is constant over the full frequency range, and correcting the spectra to account for cable inductance. Noise at lower frequencies can be reduced by performing the measurement within a Faraday cage.

4.3. Stability. Impedance is a perturbative technique and the measurement should not induce irreversible changes to the sample. Therefore, stability is a criterion for obtaining reliable impedance data. A practical issue is that impedance measurements can take several minutes, or even up to several hours, depending on the frequency range of measurement, the number of measurement points, and time required to integrate the current response. The sample must be stable during the measurement and return to its initial state after the measurement. In principle, if a sample is stable, the impedance spectrum should be reproducible and reversible. Reversible in this context means that recording the impedance spectrum from high frequency to low frequency, or low frequency to high frequency, should yield equivalent spectra.

Impedance spectroscopy, however, is often specifically applied to study the time scales of irreversible processes, such as chemical reactions and mass transport. The sample is, therefore, strictly speaking, not stable during the measurement and the measurement is not reversible. In such cases, measuring from high frequency to low frequency is good practice. At high frequencies, the modulation in electric field due to V_{ac} is too fast for slow processes to follow (e.g., ion transport). As the frequency of V_{ac} is reduced, the time scales of relevant relaxation processes emerge in the impedance spectrum. In contrast, performing the measurement from low to high frequencies may induce irreversible changes the start of the measurement, without yielding clear relaxation features in the spectrum.

4.4. Finiteness. Finally, impedance values should be finite over the frequency range of measurement.

4.5. Testing the Integrity of Impedance Data: The Kramers–Kronig (K–K) Relations. The Kramers–Kronig (K–K) relations are mathematical relationships that relate the real and imaginary components of complex functions. If either the real or imaginary part of the spectrum is known, the complementary component can be calculated using the K–K relations. This implicitly assumes that the spectrum satisfies the criteria of linearity, causality, stability, and finiteness defined above. Therefore, the K–K relations are a useful tool for checking the integrity of experimental impedance data. The K–

K transformation integrals for the real (Z_{RE}) and imaginary (Z_{IM}) components of a complex function are given by

$$Z_{IM} = \frac{2\omega}{\pi} \int_0^\infty \frac{Z_{RE}(x) - Z_{RE}(\omega)}{x^2 - \omega^2} \, dx$$

$$Z_{RE} = Z_{RE}(\infty) + \frac{2}{\pi} \int_0^\infty \frac{x Z_{IM}(x) - \omega Z_{IM}(\omega)}{x^2 - \omega^2} \, dx \quad (10)$$

A practical limitation of the K−K relations is that experimental spectra are measured over a finite frequency range, while integration is performed between the limits of 0 and ∞. A more practical approach to testing the K−K compliance of the data than applying eq 10 is introduced in the following section.

5. EQUIVALENT CIRCUIT MODELING

Equivalent circuit modeling offers a simple, visual model of complex time-dependent electrical and electrochemical processes, since it allows the impedance response of multilayer devices to be quantified through a combination of ideal−capacitors, resistors, inductors, and nonideal (CPE, Warburg) elements. The main advantage of circuit modeling is that it allows rapid analysis and comparison of different frequency spectra.

Equivalent circuit modeling is relatively easy to perform but not necessarily easy to interpret. In the field of electrochemistry, potential pitfalls of equivalent circuit modeling have been widely documented.[21−23] The main difficulty lies in finding an appropriate model, attributing physical meaning to the circuit elements, and modeling the entire frequency response of real devices with a single circuit diagram. It is instructive to understand the basics behind circuit model fitting in order to be aware of the strengths of the approach, as well as the limitations.

The majority of equivalent circuit fitting programs use a Levenberg−Marquardt algorithm,[24,25] a common approach for solving nonlinear least-squares problems. A parametrized function is fit to the experimental data by minimizing the sum of squares of the error between the simulated and the measured data points. Multiple iterations are applied to minimize the object function S, and optimize the fit parameters,[25]

$$S = \sum_{i=1}^N \omega_i \{[Z'_i - Z'_i(\omega_i, a_k)]^2 + [Z''_i - Z''_i(\omega_i, a_k)]^2\} \quad (11)$$

where ω_i is a weighting function, $Z = Z'_i - iZ''_i$ is the measured impedance data, $Z(\omega_i, a_k) = Z'_i(\omega_i, a_k) - iZ''_i(\omega_i, a_k)$ is the fitting function, and a_k ($k = 1, ..., M$) are the fitting parameters. The fit, $Z(\omega_i, a_k)$, is linearized with a Taylor expansion and the higher order terms are neglected. The function can be represented by a combination of circuit elements that account for resistive, capacitive, and inductive contributions to the impedance, i.e., the equivalent circuit diagram. The assumption is that each value of Z is linear, and therefore a combination of ideal, passive circuit elements can be used to describe the full spectrum of Z values. Nonideal elements, e.g., CPE or Warburg elements, can be incorporated into the circuit diagram to describe dispersive processes.

A disadvantage of equivalent circuit modeling is that the user must choose the circuit model, including the number, arrangement, and starting values of the circuit elements. Circuit models may be selected on the basis of knowledge of the sample

and by following more established models from the literature. Starting values for the circuit elements may be extracted or validated by other measurements, or simply guessed. A poor fit of the data indicates either an unsuitable circuit model or experimental data that do not satisfy the K−K compliance criteria.

5.1. Equivalent Circuit Modeling to Check K−K Compliance of Impedance Data. Equivalent circuit modeling offers a simple, efficient method for checking the K−K compliance of impedance data.[26,27] A single RC circuit is K−K compliant, as is a circuit composed of a series of RC elements. Therefore, any experimental data that can be fit with a series of RC elements is also K−K compliant. Further, the number of RC elements required to achieve a good fit indicates the number of relaxation processes occurring over the measured frequency range. Sometimes impedance spectra from real samples will demonstrate inductive behavior (or equivalently, negative capacitance). It is more consistent with the approach above to introduce a negative value of capacitance than to introduce an inductor in the circuit diagram when the K−K compliance of the data is checked. Negative capacitance may be related to measurement artifacts, such as long cables. However, this phenomenon has been widely reported in electrochemical cells[28] and organic solar cells.[29,30] When various offset dc voltages are applied, these effects can be studied in more detail, as these electronic processes are voltage-dependent (but cable inductance is not).

5.2. Noncompliance with K−K Relations: Blocking Contacts and Mass Transport. Noncompliance with the K−K relations may arise due to mass transport, nonhomogeneous electrode surfaces, and blocking electrodes.[1,26,27,31] These effects are not related to measurement artifacts or inaccuracies in the modeling but reflect real, physical properties of the system. In the case of mass transport (e.g., ion diffusion), a Warburg element can be used to model the impedance response. In this case, the data are K−K compliant, except at $\omega \rightarrow 0$, where $Z \rightarrow \infty$, and the data do not satisfy the criteria of finiteness.[31] Nonhomogeneous electrode surfaces (porous, rough) result in an inhomogeneous distribution of charge. In this case, the electron transfer processes at the electrode surface cannot be described with a single time constant and therefore cannot be modeled with passive, ideal circuit elements. Instead, a CPE element can be used to account for the dispersive effects.[1] Blocking electrodes result in frequency-dependent resistance and capacitance values that cannot be modeled with ideal (resistor, capacitor, inductor) or dispersive elements (Warburg, CPE) and result in nonfinite impedance values at $\omega \rightarrow 0$.[31] In this case, the frequency-range used for the fit can be reduced.

5.3. Challenges of Equivalent Circuit Modeling. Challenges in equivalent circuit modeling are related to the physical interpretation of the circuit model as well as the individual circuit elements. First, real frequency spectra may also contain interdependent relaxation processes (e.g., second-order reactions) that cannot be modeled over the full frequency range with a single circuit.[21] In this case, developing increasingly more complex circuit diagrams may improve the fit but will not shed light on the underlying physical mechanisms. Second, complex circuits can often be mathematically reduced to simpler circuits.[32] Further distinct relaxation processes that occur in parallel (i.e., on the same time scales) and can be modeled with two RC elements in parallel, i.e., $R_1 C_1$ and $R_2 C_2$. However, this circuit is mathematically equivalent to a single RC circuit with $R = R_1 + R_2$, and $1/C = 1/C_1 + 1/C_2$. So it is not possible to identify

these individual relaxation processes. Finally, it has often been shown that the frequency spectra from real devices can be modeled with a variety of different geometrical combinations of circuit elements that yield equivalent fits but do not represent a unique solution linking the frequency spectrum with a specific circuit.[21−24] Circuit modeling is therefore most effective if it is based on the physical properties of the system, and the values of the circuit elements can be corroborated with independent measurements.

Earlier work in the field of semiconductor electrochemistry, and more recently in the field of emerging PV, has made great efforts to develop analytical models that link the underlying semiconductor physics to equivalent circuit models; for example, see refs 11 and 33−35. It is impossible to survey all the work that has been done. Instead, we focus on approaches in the literature that link the physics of solar cells to basic circuit building blocks that can be more generally applied to model the impedance spectra of some electrochemical and emerging PV devices.

The advantage of developing an equivalent circuit model that accurately represents the physical properties of the solar cell is that it can be used to determine parameters such as carrier diffusion constants and mobility values and recombination rates at different operational points on the IV curve.[6,14] Further, it may be applied as a diagnostic tool to study device stability, i.e., in situ aging and degradation, and to identify materials and interfaces related to performance loss.[17,36]

5.4. Equivalent Circuit Models for Charge Transfer at Interfaces. Much early work in semiconductor electrochemistry focused on studying the electronic structure, charge transfer, and charge recombination at the semiconductor−electrolyte interface.[1,2,37] In the case of electron transfer reactions between the electrolyte and semiconductor, there are capacitance contributions of the double layer located at the electrolyte-semiconductor interface C_{DB}, the capacitance of the depletion layer formed at the semiconductor surface C_{SC}, and a resistive contribution due to the charge transfer resistance R_{CT} between the electrolyte and semiconductor. An example of a single-step electron transfer from the conduction band E_C of a semiconductor to a redox system and the corresponding equivalent circuit is shown in Figure 4.
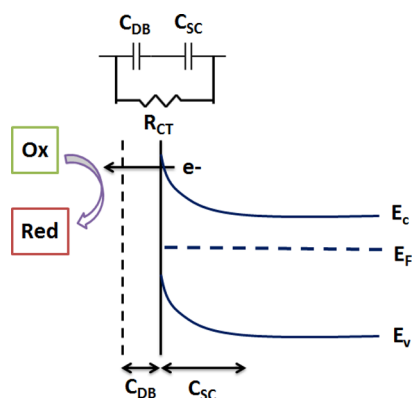

Figure 4. Equivalent circuit model for electron transfer from the conduction band E_C of a semiconductor to a redox system. C_{DB}, C_{SC}, and R_{CT}, represent the double layer capacitance, the capacitance of the depletion layer of the semiconductor, and the charge transfer resistance, respectively.

5.5. Equivalent Circuit Models for Solar Cells: Ohmic Contacts. Jamnick and Maier[33] developed a generalized equivalent circuit to represent mass and charge transport in electrical and ionic conductors subject to a time-varying electric field $E(t)$ by connecting the analytical description of carrier transport and recombination to resistive and capacitive circuit elements. In this model, charge transport in a one-dimensional conductor is considered, and carrier generation and recombination are neglected. The current density J can be represented by three distinct components:

$$J_\sigma = q\mu nE$$

$$J_{dis} = \varepsilon_o\varepsilon \frac{dE}{dt}$$

$$\nabla J_{\mu A} = -C_\mu \frac{d\mu_A}{dt} \tag{12}$$

where q is elementary charge, n is carrier density, ε is the static dielectric constant of the semiconductor, ε_o is the permittivity of free space, μ is the charge carrier mobility, μ_A is the chemical potential, and C_μ is the chemical capacitance.

The first current term, J_σ is in phase with V_{ac}. It is proportional to the conductivity of the semiconductor and describes current flow as the result of the applied voltage according to Ohm's law. It can therefore be modeled with an ideal resistor, R_{tr}, the transport resistance.

The second current term, the displacement current J_σ is 90° out of phase with V_{ac} and describes the dielectric response of the semiconductor. In the absence of free charge, a time-varying field polarizes the semiconductor. If the active layer is approximated as an ideal dielectric, this response can be modeled by introducing an ideal capacitor to account for the geometric capacitance C_{geo}

$$C_{geo} = \varepsilon\varepsilon_o \frac{A}{d} \tag{13}$$

where A is the active area and d is the thickness of the semiconductor. The value of C_{geo} can be determined by performing impedance measurements in depletion mode, i.e., in the dark under reverse bias.

The third term, ∇j_μ is the well-known continuity equation expressed in terms of the chemical potential μ_A and the chemical capacitance C_μ. The chemical capacitance, also known as the quantum capacitance, was originally introduced by Luryi to describe the capacitive contribution arising from mobile charge in a dielectric layer between two electrodes.[38] V_{ac} induces carrier injection into the distribution of electronic density of states in the dielectric, resulting in a shift in E_F. This effect manifests itself as a second capacitive contribution in series with C_{geo}. As a result, the total capacitive response of the semiconductor is lower than it would be for an ideal dielectric. For nondispersive transport, the chemical capacitance can be represented as an ideal capacitor.[33] C_μ is an extrinsic thermodynamic quantity defined as[33,39]

$$C_\mu = q^2\left(\frac{\delta G^2}{\delta^2 n}\right)^{-1}_{T,P} = q^2\left(\frac{\delta\mu_A}{\delta n}\right)^{-1}_{T,P} \tag{14}$$

where G is Gibb's free energy. In the case of semiconductors, the mobile charge are free electrons and holes, and the chemical potential is equivalent to the Fermi level, i.e., $\mu_A = E_F$, and C_μ can be expressed as[8]
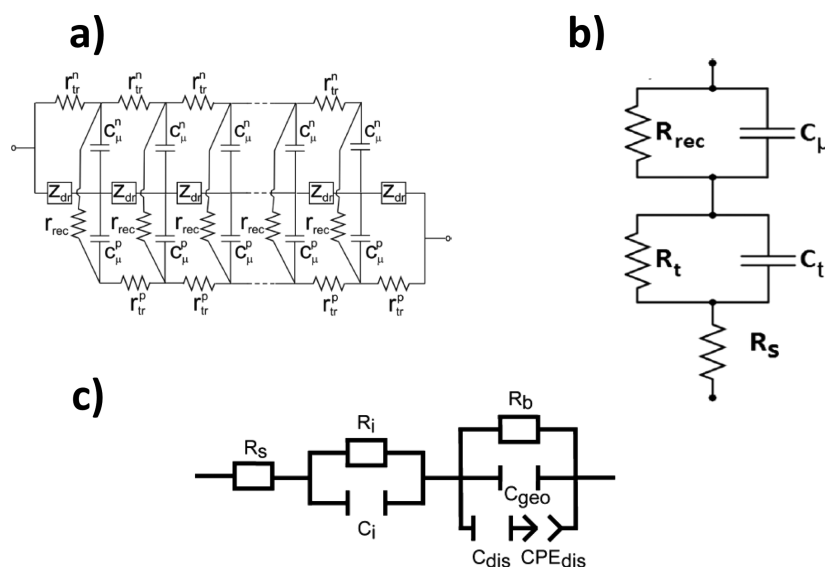
Figure 5. Examples of different equivalent circuit models for DSSC and OPV. (a) Transmission line equivalent circuit model to describe electrical or ionic conduction in a conductor with ohmic contacts. Reprinted with permission from ref 106. Copyright 2014 American Chemical Society. (b) Lumped circuit model to describe isotropic electrical transport in an organic solar cell with ohmic contacts. Reprinted with permission from ref 14. Copyright 2014 Wiley. (c) Circuit model with CPE to model organic solar cells with blocking contacts. Reprinted with permission from ref 17. Copyright 2012 American Chemical Society.

$$C_\mu = q^2 \, \frac{dn}{dE_F} \tag{15}$$

The chemical capacitance has been recognized as a key parameter for accurately modeling the performance of low dimensional semiconductors, including the electrical properties of nanostructures[40] and understanding electronic defects in 2D materials such as graphene.[41] In the case of intrinsic, thin film semiconductors (e.g., organic semiconductors), the chemical capacitance resulting from injected charge has a non-negligible impact on the impedance spectra. In contrast, inorganic and/or doped semiconductors generally have much higher carrier densities and, as a result, changes carrier density due to charge injection during the impedance measurement is insignificant, and C_μ is negligible in this case.

Bisquert[8] expanded this formalism to consider carrier generation in illuminated DSSC devices and thereby develop a model that is consistent with the basic relations that govern current flow in solar cells, i.e., the Poisson equation, continuity equation and the drift-diffusion equations. In addition to R_{tr}, C_{geo}, and C_μ this model includes an additional resistive element to account for the recombination of photogenerated charge, the recombination resistance R_{rec}. The recombination resistance has been widely used in semiconductor electrochemistry to account for the recombination of carriers,[42−44] usually at semiconductor−electrolyte interfaces. Its value depends on the generation rate of carriers (due to either injection or photogeneration) and is proportional to the recombination current j_{rec}[44]

$$R_{rec} = \frac{kT}{q j_{rec}} \tag{16}$$

Assuming a first-order, nonreversible recombination process, the carrier lifetime τ is given by[6,43]

$$\tau = R_{rec} C_\mu \tag{17}$$

Since the current flow is continuous throughout the semiconductor bulk, the resistive and capacitive elements are assumed to be distributed homogeneously, and a distributed or transmission line equivalent circuit based on building blocks consisting of $R_{tr}C_{geo}$ elements in series with $R_{rec}C_{\mu A}$ (Figure 5a) elements can be used to model the impedance spectra, also in combination with modifications to the building blocks according to the boundary conditions at the device interfaces.[6,33,34]

Impedance spectra of DSSC reveal three relaxation processes, resulting from ion diffusion in the electrolyte, electron transfer from the dye to the metal oxide, and the redox reaction at the counter electrode.[9,45] Bisquert[34] demonstrated that this seemingly complex response can be modeled considering only electron diffusion and first-order, nonreversible recombination reactions and that the impedance spectra can be described with the transmission line equivalent circuit.[11,45]

Basham et al.[14] proposed a simplification of the transmission line circuit in the form of a lumped circuit (Figure 5b) to model the impedance spectra of OPV devices based on P3HT:PCBM. The assumptions are, first, that the electrical response in the OPV active layer is isotropic, and the contacts are Ohmic. This means that the electrical transport and recombination over the whole device can be represented by single RC elements rather than a distribution of RC elements. Second, transport is much faster than recombination, and therefore, the impedance can be modeled considering two sequential relaxation processes, i.e., two RC elements in series. Their model consists of a series resistance R_s that accounts for contacting resistances, $R_{rec}C_\mu$ to account for the generation and recombination of photogenerated charge, and $R_{tr}C_{tr}$ to account for carrier transport. The carrier lifetime is given by $\tau = R_{rec}C_\mu$, and the carrier transit time τ_{tr} is defined as

$$\tau_{tr} = R_{tr} C_{tr} \tag{18}$$

and represents the time it takes for a carrier to be injected and transported across the device. C_{tr} accounts for the low carrier mobilities observed in organic semiconductors and is

determined by both C_{geo} and C_μ. At frequencies above $1/\tau_{tr}$ charge carriers can no longer follow the modulation in electric field due to the applied V_{ac}. Therefore, $f_{tr} = 1/\tau_{tr}$ represents the frequency at which the impedance transitions from resistive to capacitive. A more detailed description of the carrier transit time τ_{tr} and its relation to carrier mobility is given in section 7. The authors validated their approach by reconstructing the solar cell IV curve with the parameters extracted from the circuit model.

5.6. Equivalent Circuit Models for Solar Cells: Non-ohmic Contacts.

Ohmic contacts are often assumed for circuit modeling of solar cells; however, this is often not the case. For example, it is well-known that creating ohmic contacts in organic electronics is nontrivial.[46] In fact, performance losses in emerging PV devices are often linked to the contact interfaces. Work from my group[17] focused on developing a circuit model to describe blocking contacts in P3HT:PCBM solar cells (Figure 5c). Devices contained an amorphous titanium oxide (TiO_x) blocking layer between the active layer and cathode to simulate a degraded interface and induce an "s-shape" in the solar cell characteristics.[35] The conductivity of the TiO_x can be reversibly controlled with UV light soaking. The circuit was used to model the impedance spectra before and after light soaking and at several dc offset voltages. The first RC element accounts for the resistance and capacitance of the TiO_x interface, and the variable resistance of the TiO_x extracted from the equivalent circuit model correlates with changes in the device fill factor. The second extended RC element accounts for transport dispersive transport in the bulk organic active layer with a CPE in parallel with the geometric capacitance of the active layer C_{geo}. The circuit was later successfully applied to monitor performance loss in OPV devices prepared with different hole transport layers.[36]

These examples illustrate not only the power of the generalized approach introduced above but also some limitations. Derived from analytical expressions for carrier transport and recombination in a one-dimensional semiconductor, the diffusion–recombination model is applicable for modeling solar cells with multiple (also blocking) interfaces. The assumptions are that transport is faster than recombination and that both processes occur on well-defined, distinct time scales that are detectable in the frequency window used in impedance spectroscopy. In this case, the impedance response of the solar cell can be represented by the equivalent circuit models introduced above. Some ambiguity exists in the literature in unequivocally assigning the circuit elements to physical locations in the device, particularly in OPV devices.[14,17] This may be system-dependent, and determined by whether recombination processes are dominant at the device interfaces or in the semiconductor bulk. Variation of parameters such as contact interfaces[36] and the active layer thickness[47] can offer insight into these questions, as well as how device fabrication and geometry impacts electrical transport, and in particular, recombination.

6. CAPACITANCE–FREQUENCY (CF) MODELING

Capacitance–frequency modeling is a useful approach to analyzing impedance data if electrical transport and recombination processes occur on much faster time scales than microseconds (megahertz). It can be applied to gain insight into the electronic structure of the sample, in particular the doping density, the built-in field of the device, and the profile of electronic trap states.

The complex capacitance $\tilde{C}$ is related to the impedance Z by (see Table 2)

$$\tilde{C} = \frac{1}{(i\omega Z)} \tag{19}$$

Cf spectroscopy specifically probes electronic structure at metal–semiconductor contacts. To apply Cf spectroscopy correctly, the depletion approximation must be satisfied, meaning that there is a finite region (the space charge, or depletion, region) extending from the surface of the semiconductor into the bulk that is depleted of free charge. Note that this is generally the case in inorganic crystalline semiconductors but often not the case for mixed ion–electrical conductors, intrinsic semiconductors, and disordered semiconductors, as the mobile charge results in artifacts in the Cf spectrum.

6.1. Mott–Schottky Analysis: Passive Semiconductor–Electrode Interfaces.

The well-known Mott–Schottky relationship offers information about the built-in voltage (V_{bi}) and doping profile of the semiconductor,

$$\frac{1}{C_{SC}^2} = \frac{2}{\varepsilon\varepsilon_o qN}\left(V - V_{bi} - \frac{kT}{q}\right) \tag{20}$$

where N is the doping density and V is the applied dc voltage.

This analysis is applicable for passive semiconductor–contact interfaces, i.e., no charge injection. In this case, the total charge density in the depletion region is determined solely by the density of immobile dopants. The depletion region formed at the semiconductor-electrolyte or semiconductor-metal junction can be considered an ideal parallel plate capacitor

$$C_{SC} = \varepsilon\varepsilon_o \frac{A}{d} \tag{21}$$

where d is the width of the depletion region. In the case of semiconductor–electrolyte junctions (for example, as shown in Figure 4), the analysis assumes that the total sample capacitance is made up only by contributions from the double layer capacitance C_{DB} and C_{SC}, and that $C_{DB} \gg C_{SC}$[1] (this can be checked with circuit modeling) so that

$$\frac{1}{C_{TOT}} = \frac{1}{C_{SC}} + \frac{1}{C_{DB}} \approx \frac{1}{C_{SC}} \tag{22}$$

For solid-state devices, this is the case in reverse bias in the dark.

Under these conditions, the total device capacitance is frequency-independent over a finite range of the Cf spectrum, except at high frequencies where the series resistance dominates.

The width of the depletion layer is dependent on the applied dc voltage (eq 20), so from a plot of $\frac{1}{C^2}$ vs V, the values of N and V_{bi} can be extracted from the slope and intercept, respectively. It follows that in the case of n-doping the slope is positive, while for p-doping the slope is negative.

The Mott–Schottky analysis has become standard in solid-state solar cells. However, in the case of low doping concentrations and/or very thin films (e.g., OSC) the semiconductor may not be fully depleted during the measurement, and the chemical capacitance C_μ resulting from injected carriers contributes to the total capacitive response.[48,49] As a result, the analysis overestimates the C_{SC}, therefore yielding incorrect values for N and V_{bi}. Kirchartz et al.[48] performed a systematic study combining simulation and experiment to identify conditions that allow accurate Mott–Schottky analysis on OPV devices. Ion migration in perovskite PV has also been

identified as a source of error in the Mott−Schottky analysis, due to the additional (strongly frequency-dependent) contribution of mobile ions to the capacitance spectrum.[50]

6.2. Defect Spectroscopy. An important part of photovoltaic research is studying the influence of electronic defects on photovoltaic performance. This involves characterizing the density and distributions of electronic trap states in the semiconductor, and at semiconductor−electrode interfaces. Defect spectroscopy probes the capacitive contribution of trap states as a function of temperature and/or voltage in order to determine the trap energy with respect to the semiconductor band edges. Deep level transient spectroscopy (DLTS) and (often in combination with) admittance spectroscopy are the most common techniques used for defect spectroscopy.[51−59] DLTS[51] is a very sensitive technique to determine trap energy, density, and distribution in the bandgap. However, DLTS relies on the fact that the width of the depletion region can be controlled by the applied voltage, which is generally satisfied in the case of crystalline, highly doped semiconductors and pn junction or Shottky junction devices but not in the case of many emerging PV devices based on amorphous, very thin, and/or with low doping densities, and multiple device interfaces[52,60] where the depletion region extends throughout the bulk of the material and the chemical capacitance from injected charge is not negligible.

Walter et al.[52] introduced a simple approach to model defect distributions in the bandgap of Cu In(Ga)Se$_2$ solar cells using admittance spectra. This approach was later extended to OPV[57−59] and perovskite solar cells.[54,61] The model assumes that the only contribution to device capacitance results from the occupation/emission from defect states.[52,57] Figure 6 shows a
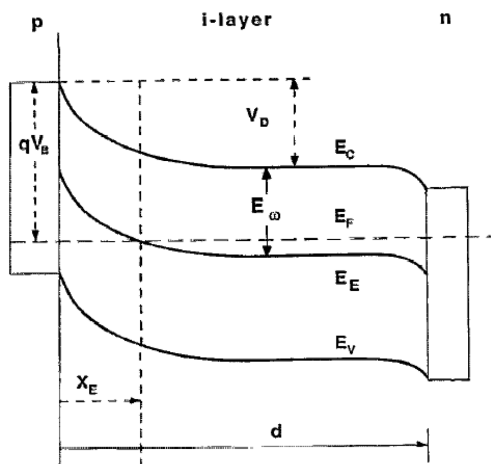
Figure 6. Band diagram of a p-i-n junction, where V_D is the band bending at the junction, E_c is the conduction band, E_v is the valence band, E_F is the Fermi level, X_E is the width of the p-i junction, d is the width of the device, V_B is the built-in field, E_E represents the center of the trap distribution, and E_ω is the demarcation energy that separates traps that respond to V_{ac} at frequency ω from those that do not. Reprinted with permission from ref 62. Copyright 1992 AIP.

model p-i-n junction with a Schottky junction at the p-i contact, and an ohmic i-n contact.[62] The width of the depletion region is given by X_E and d is the width of the device. During the measurement, the V_{ac} probes the filling/emptying of defect states in the depletion region within a defect distribution E_E with energies in the vicinity of E_F.[62]

The characteristic time scale τ_{trap} for thermal emission of a carrier from a defect is given by[52,57,62]

$$\tau_{trap} = \gamma^{-1} \exp\left(\frac{\Delta E}{kT}\right) \tag{23}$$

where γ is the attempt to escape frequency and ΔE is the energy difference between the defect site and band edge. During the measurement, τ_{trap} is probed by sweeping the frequency of V_{ac}, as there is a maximum frequency at which the defect responds to the voltage modulation. In other words, τ_{trap} corresponds to a characteristic frequency $\omega_{trap} = 2\pi f_{trap}$ and eq 23 can be rewritten as

$$\Delta E = E_\omega = kT \ln\left(\frac{\gamma}{\omega_{trap}}\right) \tag{24}$$

where E_ω represents a demarcation energy that separates defect states that respond to the voltage modulation at frequency ω_{trap} and those that do not.

The density of defect states DOS$_{trap}$ is assumed to be proportional to the derivative of the device capacitance with respect to frequency[36,52,57,58]

$$DOS_{trap}(E) = \frac{-V_{bi}\omega}{qdkT} \frac{\delta C}{\delta \omega} \tag{25}$$

This analysis alone does not reveal the identify the nature of the traps, as the sign of ΔE is not defined. In the literature, it is common to assume a symmetric trap distribution (e.g., parabolic[52] or Gaussian[36,57,58]) centered around a peak energy, e.g., E_E. Temperature-dependent measurements are required to determine the defect activation energy E_A and attempt-to-escape frequency γ to obtain accurate results for the energetic position of the defect distribution within the bandgap.

Since the analysis assumes that the only contribution to device capacitance comes from the populating/depopulating of trap states, other contributions to device capacitance will result in artifacts in the DOS$_{trap}$ distribution. For example, Hsu and co-workers[57] showed that in OPV devices with thick active layers and/or at low applied dc voltages, a capacitive contribution at higher frequencies is observed, resulting in the appearance of a shallow traps in the DOS$_{trap}$. This artifact was attributed to the low carrier mobilities, i.e., carriers with long transit times that cannot follow the modulation of the voltage at high frequencies (see previous section), i.e., "carrier freeze-out". As a result, there is a contribution from the geometric capacitance C_{geo} at higher frequencies. This is illustrated in Figure 7a where the Cf spectrum demonstrates a high frequency artifact that depends on the thickness of the semiconductor layer, i.e., increasing with increasing OSC thickness. In Figure 7b the experimental data for the DOS$_{trap}$ distribution as well as the results from the Gaussian fit are shown. Kirchartz and co-workers[63] recently confirmed these results and demonstrated that in low mobility materials, where time scales for charge transport are slower than time scales for trap emission, the analysis may yield incorrect results for the defect activation energy E_A and attempt-to-escape frequency γ.

6.3. Permittivity Spectrum and the Dielectric Constant. The permittivity ε can be determined from the complex capacitance $\tilde{C}$ and impedance Z according to (see Table 2)

$$\varepsilon = C_o \tilde{C} = i\omega C_o Z \tag{26}$$
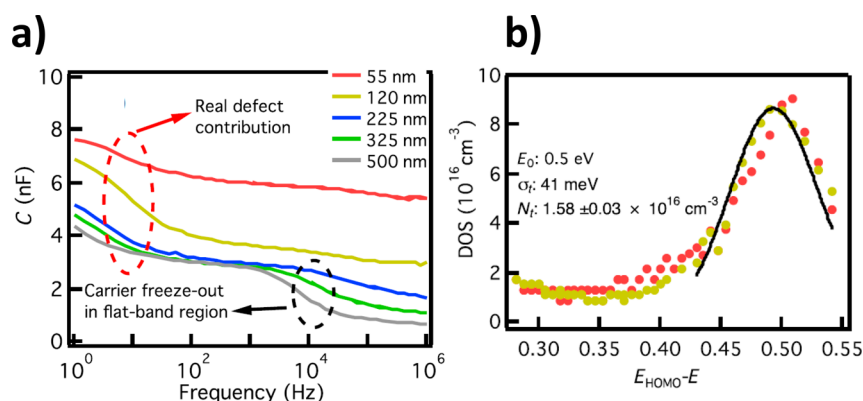
Figure 7. (a) Cf spectrum for OPV with layer thicknesses varying from 55 to 500 nm. The low frequency feature in the spectrum is attributed to real trap states. The thickness-dependent feature at higher frequencies is attributed to low carrier mobility, i.e., carrier freeze-out. (b) The density of trap states, DOS_{trap}. The experimental data (symbols) are fit with a Gaussian distribution (solid line). Reprinted with permission from ref 57. Copyright 2016 by the American Physical Society.

To do this, the capacitance of the empty cell C_o, which is defined by the geometry of the sample, must be known. The permittivity is, of course, also a complex parameter. The real component of the permittivity, ε', is often referred to simply as the permittivity and describes the storage of electrical energy by the sample. The dielectric loss ε'' describes the dissipation of electrical energy by the sample. Note that this follows from eq 26, as ε' is actually an imaginary parameter (it can be represented by an ideal capacitor) while ε'' a real parameter (it can be represented by an ideal resistor) when plotted in the complex plane (Figure 2). The angle φ between the real and imaginary components of the permittivity is known as the loss tangent.

Ideal dielectric relaxation from the reorientation of bound dipoles moments results in an increase in values of ε' at frequencies $< \omega_p = \tau^{-1}$, and a corresponding peak at $\omega_p = \tau^{-1}$ in the ε'' spectrum (Figure 1). In the case of conductive samples, however, ε'' is predicted to increase with a characteristic 1/frequency signature,[3] as dielectric loss is a dissipative parameter that is directly proportional to the conductivity σ of mobile charge

$$\varepsilon'' = \frac{\sigma}{\omega \varepsilon_o} \tag{27}$$

The Debye equation predicts the permittivity spectrum for an ideal relaxation due to a collection of noninteracting, fixed dipoles with a single relaxation time constant τ

$$\varepsilon(\omega) = \varepsilon_\infty + \frac{\varepsilon_s - \varepsilon_\infty}{1 + i\omega\tau} \tag{28}$$

where ε_s is the dielectric constant or static permittivity. It represents the case at $\omega \to 0$, in which the sample is in equilibrium with the electric field. ε_∞ is the high frequency dielectric permittivity at $\omega \to \infty$. Cole and Cole[64] expanded this approach to describe dipole relaxation with a distribution of time scales

$$\varepsilon(\omega) = \varepsilon_\infty + \frac{\varepsilon_s - \varepsilon_\infty}{1 + (i\omega\tau)^\alpha} \tag{29}$$

where $0 < \alpha < 1$. If $\alpha = 1$, then the Cole–Cole equation reduces to the Debye equation. Further generalizations of the Debye equation have been proposed (e.g., Havrikliak–Negami[65]) to account for deviations from ideal dielectric response.[66]

Real dielectrics very frequently yield permittivity spectra that do not follow these predictions. Jonscher's "universal law of dielectrics"[4,67] describes the general behavior of many classes of dielectrics that demonstrate very similar dielectric responses, but deviating markedly from that predicted by Debye.[68]

In research on emerging photovoltaics, the permittivity spectrum is often neglected, though the dielectric constant ε_s of the semiconductor is considered to be relevant, as it has been related to charge recombination. For example, in OPV, increased Coulombic interactions between charge carriers in molecular semiconductors with low dielectric constants (typically $\varepsilon_s = 3$)[69] has been linked to recombination losses.[70] Researchers in this field have been investigating strategies to chemically design materials with higher dielectric constants.[71]

It is not straightforward to determine reliable values for ε_s in thin film semiconductors[72] using impedance spectroscopy, and many practical considerations are required. For one, the additional capacitive contributions from contact layers and device interfaces must be accounted for. This may be done with equivalent circuit modeling, assuming that the capacitive contribution from the active layer can be identified and quantified. Further, it has been shown that the porosity of the contact must be considered in thin film devices to obtain accurate effective areas for the device geometry, and therefore values of ε_s.[73] Additionally, contributions from the chemical capacitance (OPV) and mobile ions (perovskites) will complicate the analysis, as these signatures result in features in the permittivity spectrum. Particularly in the case of perovskites, strong frequency-dependence in the low frequency regime of the spectrum as $\omega \to 0$, resulting from ionic conduction and electrode polarization,[74] have made it difficult to experimentally determine reliable values for ε_s.[75,76] For example, high reported values for dielectric constants (e.g., $\varepsilon_s = 60$) have been attributed to nonequilibrium processes, such as ionic conductivity combined with lattice interactions and distortions.[74,77–79]

On a more general note, the static permittivity is significant only when the solar cell can be considered to be in equilibrium. However, the permittivity and dielectric loss spectra contain a wealth of information about nonequilibrium processes, such as the ultrafast separation of photogenerated charge,[80] and structural dynamics on slower time scales, such as dipole reorganization.[81] Cooperation between researchers applying techniques that probe the permittivity spectrum over a wider range of frequencies, e.g., impedance spectroscopy, dielectric spectroscopy, and terahertz spectroscopy, may reveal interesting

insights here,[82] particularly on the time scales of underlying structural mechanisms related to energy conversion.

7. MOBILITY MEASUREMENTS AND TRANSPORT STUDIES

7.1. Mobility Measurements on Organic Semiconductors. Carrier mobility and lifetime are key material parameters for photovoltaic performance. However, determining reliable carrier mobility values in low mobility materials with inherently high structural and/or energetic disorder,[83] such as organic semiconductors (OSC), is often nontrivial. Carrier mobility in OSC has been reported to depend on carrier density, electric field, and temperature, and therefore on device structure and measurement parameters.[84]

"Steady-state" approaches, such as space charge limited current (SCLC) analysis can be applied to extract carrier mobility on unipolar, pristine OSC layers in "single carrier diode" architectures with nonblocking contacts.[85,86] Field effect transistor (FET) mobility measurements enable the study of electron and hole transport in the same device,[87] allowing insight into how processing of the active layer influences carrier transport.[88] Further the planar, thin film FET structures are useful for studying the efficiency of charge injection and extraction at device contacts.[89] However, the transistor architecture and measurement conditions are markedly different than standard solar cell testing conditions and may yield different mobility values.[90] Further, steady-state approaches offer very limited insight into dispersive (time-dependent) effects impacting carrier transport, i.e., due to electronic disorder and trapping.

Transient current techniques, such as such as time-of-flight (TOF),[83] charge extraction with linear increasing voltage (CELIV)[91] and transient photocurrent (TPC) or photovoltage (TPV),[92] and time delayed collection field (TdcF),[93] offer the advantage that the measurement can be performed on solar cell architectures, and dispersive transport and recombination processes can be characterized. ToF, however, requires thick, pristine OSC layers, and the analysis of the transients is error-prone due to the dispersive nature of carrier transport in OSC.[83] In contrast, CELIV, TPC, and TPV can be performed on solar cells under relevant operating conditions. However, in addition to the transient current response from charge carriers, the time-varying electric field also induces a displacement current due to the dielectric response of the OSC (see eq 12). Therefore, the RC time constant of the circuit must be well-known (and ideally minimalized) to extract accurate mobility values from the current transients.[94,95] Further, for most transient current techniques (with the exception of i-CELIV[91]) only the fastest carriers contribute to the transients, and it is not possible to study electron and hole transport independently in the same device. Time scales of transport and recombination phenomena can also be extracted from impedance and admittance spectra.[6] The advantage in this case is that the RC constant of the circuit can easily be determined and accounted for with circuit modeling, and the mobility of both electron and holes can be determined in a single measurement.[96]

7.2. Determining Carrier Mobility from Admittance Spectra on Space Charge Limited Diodes. The use of impedance spectroscopy to extract carrier mobility values from OSC diodes in the dark is outlined here. Measurements are performed in the dark, assuming space charge limited transport as OSC are inherently intrinsic, and at low voltages (and in the dark) there are no thermal carriers. For $V > V_{bi}$, carriers are injected into the diode, and if one contact is ohmic (injection) and the other is blocking, then the current density follows Child's law and is given by[97]

$$j = \frac{9}{8}\varepsilon\varepsilon_o\mu\frac{V^2}{d^3} \tag{30}$$

where μ is the carrier mobility and d is the thickness of the semiconductor layer. During the impedance measurement, the V_{ac} input is used to probe the time scale of charge injection followed by the redistribution of space charge in the bulk of the OSC. This yields the carrier transit time, and can be used to calculate carrier mobility.

The following derivation is given in more detail in refs 98 and 99, and I follow their notation here. For the small signal ac measurement, the steady-state and time-dependent contributions can be separated by introducing time-dependent components for electric field E, charge density ρ, and current density J

$$j(t) = q\mu(t)\,\rho_{dc}e(x,t) + \varepsilon\mu(t)E_{dc}\frac{\delta e(x,t)}{\delta x} + \varepsilon\frac{\delta e(x,t)}{\delta t} \tag{31}$$

The three contributions to $j(t)$ are the (1) dc current (2) time-dependent injection of charge, and (3) displacement current combined with the relaxation of space charge in the bulk. Using eq 31 and applying a Fourier transform (assuming an electric-field-independent mobility μ) to solve for admittance Y yield

$$Y(\Omega) = \frac{\varepsilon A}{\tau_{tr}d} \times \left(\frac{\Omega^3}{2i[0.75\tilde{\mu}(\Omega)]^2(1 - \exp[-i4\Omega/3\tilde{\mu}(\Omega)]) + 1.5\tilde{\mu}(\Omega)\Omega - i\Omega^2}\right) \tag{32}$$

where A is the active area of the device and $\Omega = 2\pi f\tau_{trans}$. At high frequencies ($\Omega \gg 1$) carriers no longer follow the ac modulation, and $Y \approx \frac{\varepsilon A}{d} = C_{geo}$. The carrier transit time τ_{trans} is the time scale for carrier injection and the resulting rearrangement of space charge. Note that, here, τ_{trans} is explicitly differentiated from τ_{tr} in eq 18. Both time scales represent carrier transit times; however, τ_{tr} represents the time scale of carrier diffusion in the illuminated solar cell, while τ_{trans} is related to the carrier drift mobility.

The frequency-dependent carrier mobility $\mu(\Omega)$ takes into account dispersive transport effects due to hopping[98] or trapping.[100] In other words, injected carriers have an initially higher mobility, which decreases in time. The dc mobility μ_{dc} reflects steady-state transport at longer time scales. The slowing down of carriers is accounted for by the normalized mobility $\tilde{\mu}(\Omega)$, i.e., the ratio between the frequency-dependent mobility and the dc mobility,

$$\tilde{\mu}(\Omega) = \frac{\mu(\Omega)}{\mu_{dc}} = 1 + M(i\Omega)^{1-\alpha} \tag{33}$$

where M and α are dispersion parameters that relate the ac mobility to the dc mobility.

The steady-state carrier mobility μ_{dc} is related to the dc carrier transit time τ_{dc} by[99,101]

$$\tau_{dc} = \kappa\frac{d^2}{(V - V_{bI})\mu_{dc}} \tag{34}$$

where K is a constant that relates the ac transit time τ_{trans} in eq 32 to an average dc transit time τ_{dc}, and Tsang et al.[99] found values of $\tau_{\text{dc}} \approx 0.56\tau_{\text{trans}}$ for both dispersive and nondispersive transport. Signatures of dispersive transport can be identified by fitting the impedance spectrum with an equivalent circuit model composed of an R-CPE circuit. If $n = 1$, the CPE reduces to an ideal capacitor, and the transport is not dispersive.[18]

Extracting the carrier transit time from the admittance spectra is relatively straightforward due to the clear signature of slow carriers in the complex capacitance $\tilde{C}$ spectrum and the susceptance $B(\omega)$ spectra, where $Y = G - iB$. At low voltages ($V < V_{\text{bi}}$), no charge is injected, and the geometric capacitance C_{geo} of the OSC dominates the spectrum. At higher voltages ($V > V_{\text{bi}}$) charge is injected, resulting in a redistribution of space charge. At high frequencies ($f > \tau_{\text{tr}}^{-1}$), the modulation in the electric field from V_{ac} is too fast for carriers to follow and the capacitance spectrum is dominated by C_{geo}. At low frequencies ($f < \tau_{\text{tr}}^{-1}$) the injection of charge lags behind the modulation in electric field induced by V_{ac}, resulting in a drop in capacitance. The frequency at the crossover between these two regimes corresponds to the ac transit time of the carriers, $f_{\text{tr}} = \tau_{\text{tr}}^{-1}$. This behavior is shown in Figure 8, which depicts
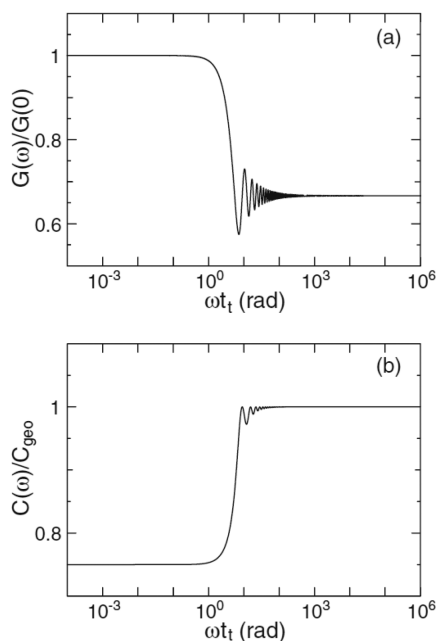

Figure 8. Simulations of the normalized (a) conductance $G(\omega)/G_{\text{o}}$ and (b) capacitance $C(\omega)/C_{\text{geo}}$ as a function of angular frequency ω. Reprinted with permission from ref 103. Copyright 2008 The Japan Society of Applied Physics.

simulations of the influence of carrier transport on the normalized conductivity, $G(\omega)/G_{\text{o}}$, and the normalized capacitance, $\tilde{C}/C_{\text{geo}}$. Plotting the differential susceptance B versus frequency, $-\Delta B = -\omega(\tilde{C} - C_{\text{geo}})$, results in a peak at the crossover frequency. This representation facilitates the extraction of τ_{tr} from the data, and the dc carrier mobility can be calculated from eq 34.

Martens et al.[98] first demonstrated this approach to study hole transport in poly(p-phenylenevinylene) (PPV) diodes. They later extended the analysis to study ambipolar transport in PPV light emitting diodes,[96] as electron and hole transport results in two independent peaks in the $-\Delta B$ versus frequency spectrum. Berleb et al.[100] extended the analysis to include field-dependent

mobility and trapping with studies on tris(8-hydroxyquinoline)-aluminum (Alq$_3$) diodes. Gommans et al.[102] demonstrated that the same analysis could be performed on PPV diodes by assuming a field-independent mobility and including a distribution of trap sites to account for dispersive transport.

The C spectrum often contains additional features in the low and high frequency range, not related to electrical transport. Many experimental studies have revealed a strongly frequency-dependent capacitance at low frequencies. Okachi et al.[103] combined experimental studies with simulations and attributed increasing capacitance with decreasing frequency to trap states in the OSC, while Tsang et al.[99] attributed the same behavior to dispersive transport. Negative values of capacitance at low frequencies in ambipolar devices has been attributed to recombination.[29,30] Past theoretical studies have shown that hopping transport in a distribution of localized energetic sites is mathematically equivalent to band transport with multiple trapping and release,[104,105] which may account for the consistency of the analysis and results between these studies, despite discrepancies in the interpretations regarding the field dependence of the mobility and the effects of carrier trapping. High frequency-dependent features in capacitance spectrum have also been attributed to dielectric relaxation of polymer films.[98,102]

7.3. Determining Carrier Mobility from Impedance Spectra. To circumvent artifacts in the analysis, Tripathi et al.[101] demonstrated that the $-Z''$ spectrum yields a clearer signature of electrical transport than the $\tilde{C}$ or B spectra. Figure 9
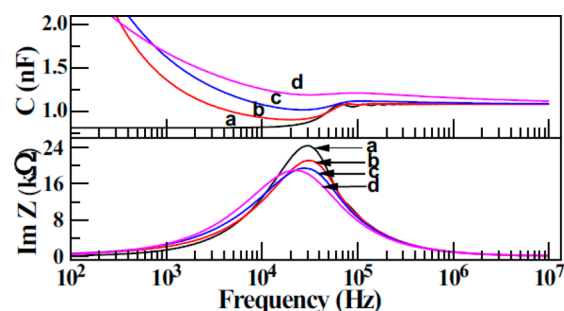

Figure 9. Comparisons of simulated spectra of normalized capacitance C/C_{geo} (top) and the normalized $-Z''$ (here depicted as Im Z) (bottom) versus frequency for increasingly dispersive transport (M, α). Lines: (a) nondispersive, (b) low dispersion, (c) moderate dispersion, and (d) highly dispersive. Reprinted with permission from ref 101. Copyright 2011 AIP.

shows the comparison of the simulated spectra of the capacitance and $-Z''$ spectrum (labeled as Im Z) for various degrees of dispersion in the transport. The mobility can now be extracted using eq 34, by equating the transit time τ_{trans} to the peak frequency in the plot.

In a comparative study of different mobility measurement techniques used in organic electronics, Clarke et al.[13] found that impedance spectroscopy yields mobility values consistent with other steady-state and transient techniques. However, mobility values extracted using impedance are ubiquitously lower. This is attributed to the fact that the transit time extracted with this approach includes the time scale required for carrier injection as well as charge transport.

8. SUMMARY

Research in emerging PV is highly interdisciplinary and combines expertise from synthetic chemistry, physical chemistry, solid-state physics, material science, and engineering. It is difficult for beginners from different backgrounds to develop a comprehensive overview of how impedance spectroscopy can be applied to characterize new photovoltaic materials and devices. One challenge is that the electrochemical community generally applies equivalent circuits to model impedance spectra, while the solid-state community more commonly uses Cf analyses. The underlying assumptions and general applicability of these approaches are different and are not easily accessible from the literature. My goal in this review was therefore to unify the common analysis frameworks used in the field, along with the underlying assumptions, limitations, and potential pitfalls, in a single manuscript. This, hopefully, provides researchers with a general toolbox to study new photovoltaic materials with impedance spectroscopy.

Broader understanding of the physical assumptions behind each analysis enables a more versatile application of the technique. For example, equivalent circuit modeling and Cf spectroscopy can be combined to elucidate different parameters. In the case of perovskite PV, equivalent circuit modeling can be used to identify and quantify the slow transport of ions with models incorporating Warburg or CPE elements, while Cf measurements can be used to characterize electronic properties of the perovskite, such as doping densities and trap profiles at device contacts. In this case, performing the measurements at low temperatures will limit the contribution of ion transport to the Cf spectrum.

I focus mainly on OSC in this review, however, the approaches introduced here are valid for other low mobility, amorphous semiconductor—combining equivalent circuit modeling with transport studies can be used to study carrier drift and diffusion, as well as identify signatures of dispersive transport related to energetic disorder and trapping.

More general cases may involve studying charge injection and extraction at semiconductor—metal interfaces, for example, with circuit models to identify blocking or porous contacts, and combining this analysis with Cf spectroscopy to study electronic structure.

While impedance spectroscopy is an old and well-established technique, it takes time to master. This may be worth the effort due to the development of new photovoltaic technologies. Further, interesting synergies with other research fields may open up new perspectives for applying impedance spectroscopy in a new paradigm of material science. While impedance spectroscopy has traditionally been used on macroscopic systems, it can easily be combined with microscopy for increased spatial resolution to locally probe sample conductivity and electronic structure or with optical spectroscopy to correlate optoelectronic properties of photovoltaic materials with processes of charge separation and transport, as well as material structural dynamics.

AUTHOR INFORMATION

Corresponding Author
*E-mail: e.l.von.hauff@vu.nl.

ORCID
Elizabeth von Hauff: 0000-0002-6269-0540

Notes
The author declares no competing financial interest.

Biography

Photo by Elizabeth von Hauff

Elizabeth von Hauff studied Physics at the University of Alberta in Edmonton, Canada. Her Ph.D. work was at the University of Oldenburg, Germany, with a focus on charge carrier transport in organic semiconductors. In 2011 Elizabeth completed her habilitation in experimental physics and then accepted a joint appointment as Associate Professor between the Institute of Physics at the University of Freiburg and the Fraunhofer Institute for Solar Energy Systems (ISE). In 2013 Elizabeth was appointed Associate Professor in Physics at the VU Amsterdam. She is interested in fundamental questions in physics and chemistry within the context of real applications.

◼ ACKNOWLEDGMENTS

◼ REFERENCES

(1) Lvovich, V. F. *Impedance Spectroscopy: Applications to Electrochemical and Dielectric Phenomena*; John Wiley & Sons, 2012.

(2) *Impedance Spectroscopy: Theory, Experiment, and Applications*, 2nd ed.; Barsoukov, E., Macdonald, J. R., Eds.; Wiley, 1995.

(3) Froehlich, H. *Theory of Dielectrics*; Oxford University Press: Oxford, 1949.

(4) Jonscher, A. K. *Dielectric Relaxation in Solids*; Chelsea Dielectrics Press: London, 1983.

(5) Sacco, A. Electrochemical Impedance Spectroscopy: Fundamentals and Application in Dye-Sensitized Solar Cells. *Renewable Sustainable Energy Rev.* **2017**, *79*, 814−829.

(6) Fabregat-Santiago, F.; Garcia-Belmonte, G.; Mora-Seró, I.; Bisquert, J. Characterization of Nanostructured Hybrid and Organic Solar Cells by Impedance Spectroscopy. *Phys. Chem. Chem. Phys.* **2011**, *13*, 9083−9118.

(7) Pascoe, A. R.; Duffy, N. W.; Scully, A. D.; Huang, F.; Cheng, Y.-B. Insights into Planar $CH_3NH_3PbI_3$ Perovskite Solar Cells Using Impedance Spectroscopy. *J. Phys. Chem. C* **2015**, *119*, 4444−4453.

(8) Bisquert, J. Chemical Capacitance of Nanostructured Semiconductors: Its Origin and Significance for Nanocomposite Solar Cells. *Phys. Chem. Chem. Phys.* **2003**, *5*, 5360−5364.

(9) Kern, R.; Sastrawan, R.; Ferber, J.; Stangl, R.; Luther, J. Modeling and Interpretation of Electrical Impedance Spectra of Dye Solar Cells Operated under Open-Circuit Conditions. *Electrochim. Acta* **2002**, *47*, 4213−4225.

(10) Quintana, M.; Edvinsson, T.; Hagfeldt, A.; Boschloo, G. Comparison of Dye-Sensitized ZnO and TiO2solar Cells: Studies of

Charge Transport and Carrier Lifetime. *J. Phys. Chem. C* **2007**, *111*, 1035.

(11) Adachi, M.; Sakamoto, M.; Jiu, J.; Ogata, Y.; Isoda, S. Determination of Parameters of Electron Transport in Dye-Sensitized Solar Cells Using Electrochemical Impedance Spectroscopy. *J. Phys. Chem. B* **2006**, *110*, 13872−13880.

(12) Tiwana, P.; Docampo, P.; Johnston, M. B.; Snaith, H. J.; Herz, L. M. Electron Mobility and Injection Dynamics in Mesoporous ZnO, SnO$_2$, and TiO$_2$ Films Used in Dye-Sensitized Solar Cells. *acS Nano* **2011**, *5*, 5158−5166.

(13) Clarke, T. M.; Lungenschmied, C.; Peet, J.; Drolet, N.; Mozer, A. J. A Comparison of Five Experimental Techniques to Measure Charge Carrier Lifetime in Polymer/Fullerene Solar Cells. *Adv. Energy Mater.* **2015**, *5*, 1401345.

(14) Basham, J. I.; Jackson, T. N.; Gundlach, D. J. Predicting the J-V Curve in Organic Photovoltaics Using Impedance Spectroscopy. *Adv. Energy Mater.* **2014**, *4*, 1400499.

(15) Yuan, Y.; Huang, J. Ion Migration in Organometal Trihalide Perovskite and Its Impact on Photovoltaic Efficiency and Stability. *Acc. Chem. Res.* **2016**, *49*, 286−293.

(16) Warburg, E. Ueber Das Verhalten Sogenannter Unpolarisirbarer Elektroden Gegen Wechselstrom. *Ann. Phys.* **1899**, *303*, 493−499.

(17) Ecker, B.; Egelhaaf, H. J.; Steim, R.; Parisi, J.; von Hauff, E. Understanding S-Shaped Current-Voltage Characteristics in Organic Solar Cells Containing a TiO x Interlayer with Impedance Spectroscopy and Equivalent Circuit Analysis. *J. Phys. Chem. C* **2012**, *116*, 16333−16337.

(18) Tchamba Yimga, N.; Ramanan, C.; Borchert, H.; Parisi, J.; Untenecker, H.; Kirsch, P.; von Hauff, E. Interplay between Long-Range Crystal Order and Short-Range Molecular Interactions Tunes Carrier Mobility in Liquid Crystal Dyes. *acS Appl. Mater. Interfaces* **2017**, *9*, 6228−6236.

(19) Veal, B. W.; Baldo, P. M.; Paulikas, A. P.; Eastman, J. A. Understanding Artifacts in Impedance Spectroscopy. *J. Electrochem. Soc.* **2015**, *162*, H47−H57.

(20) Fasmin, F.; Srinivasan, R. Review—Nonlinear Electrochemical Impedance Spectroscopy. *J. Electrochem. Soc.* **2017**, *164*, H443−H455.

(21) Harrington, D. A.; Van Den Driessche, P. Mechanism and Equivalent Circuits in Electrochemical Impedance Spectroscopy. *Electrochim. Acta* **2011**, *56*, 8005−8013.

(22) Macdonald, D. D. Review of Mechanistic Analysis by Electrochemical Impedance Spectroscopy. *Electrochim. Acta* **1990**, *35*, 1509−1525.

(23) Zoltowski, P. A New Approach to Measurement Modelling in Electrochemical Impedance Spectroscopy. *J. Electroanal. Chem.* **1994**, *375*, 45−57.

(24) Macdonald, J. R. Impedance Spectroscopy: Old Problems and New Developments. *Electrochim. Acta* **1990**, *35*, 1483−1492.

(25) Boukamp, B. A. Impedance Spectroscopy, Strength and Limitations. *Tech. Mess.* **2004**, *71*, 454−459.

(26) Agarwal, P. Measurement Models for Electrochemical Impedance Spectroscopy. *J. Electrochem. Soc.* **1992**, *139*, 1917.

(27) Boukamp, B. A. A Linear Kronig-Kramers Transform Test for Immittance Data Validation. *J. Electrochem. Soc.* **1995**, *142*, 1885.

(28) Jonscher, A. K. *J. Chem. Soc., Faraday Trans. 2* **1986**, *82*, 75−81.

(29) Niu, Q.; Crăciun, N. I.; Wetzelaer, G. J. A. H.; Blom, P. W. M. Origin of Negative Capacitance in Bipolar Organic Diodes. *Phys. Rev. Lett.* **2018**, *120*, 116602.

(30) Ehrenfreund, E.; Lungenschmied, C.; Dennler, G.; Neugebauer, H.; Sariciftci, N. S. Negative Capacitance in Organic Semiconductor Devices: Bipolar Injection and Charge Recombination Mechanism. *Appl. Phys. Lett.* **2007**, *91*, 012112.

(31) Van Meirhaeghe, R. L.; Dutoit, E. C.; Cardon, F.; Gomes, W. P. On the Application of the Kramers-Kronig Relations to Problems Concerning the Frequency Dependence of Electrode Impedance. *Electrochim. Acta* **1975**, *20*, 995−999.

(32) Macdonald, J. R. Analysis of Immittance Spectroscopy Data: Model Comparisons, Universality?, and Estimation of Distributions of Activation Energies. *MRS Online Proc. Libr.* **1995**, *411*, 71−83.

(33) Jamnik, J.; Maier, J. Generalised Equivalent Circuits for Mass and Charge Transport: Chemical Capacitance and Its Implications. *Phys. Chem. Chem. Phys.* **2001**, *3*, 1668−1678.

(34) Bisquert, J. Theory of the Impedance of Electron Diffusion and Recombination in a Thin Layer. *J. Phys. Chem. B* **2002**, *106*, 325−333.

(35) Glatthaar, M.; Riede, M.; Keegan, N.; Sylvester-Hvid, K.; Zimmermann, B.; Niggemann, M.; Hinsch, A.; Gombert, A. Efficiency Limiting Factors of Organic Bulk Heterojunction Solar Cells Identified by Electrical Impedance Spectroscopy. *Sol. Energy Mater. Sol. Cells* **2007**, *91*, 390−393.

(36) Ecker, B.; Posdorfer, J.; von Hauff, E. Influence of Hole Extraction Efficiency on the Performance and Stability of Organic Solar Cells. *Sol. Energy Mater. Sol. Cells* **2013**, *116*, 176−181.

(37) Gomes, W. P.; Vanmaekelbergh, D. Impedance Spectroscopy at Semiconductor Electrodes: Review and Recent Developments. *Electrochim. Acta* **1996**, *41*, 967−973.

(38) Luryi, S. Quantum Capacitannce Devices. *Appl. Phys. Lett.* **1988**, *52*, 501−503.

(39) Pelton, A. D. The Chemical Capacitance - a Thermodynamic Solution Property. *J. Chim. Phys. Phys.-Chim. Biol.* **1992**, *89*, 1931−1949.

(40) John, D. L.; Castro, L. C.; Pulfrey, D. L. Quantum Capacitance in Nanoscale Device Modeling. *J. Appl. Phys.* **2004**, *96*, 5180−5184.

(41) Xia, J.; Chen, F.; Li, J.; Tao, N. Measurement of the Quantum Capacitance of Graphene. *Nat. Nanotechnol.* **2009**, *4*, 505−509.

(42) van den Meerakker, J. E. A. M.; Kelly, J. J.; Notten, P. H. L. The Minority Carrier Recombination Resistance: A Useful Concept in Semiconductor Electrochemistry. *J. Electrochem. Soc.* **1985**, *132*, 638−642.

(43) Goossens, A.; Schoonman, J. The Impedance of Surface Recombination at Illuminated Semiconductor Electrodes: A Non-Equilibrium Approach. *J. Electroanal. Chem. Interfacial Electrochem.* **1990**, *289*, 11−27.

(44) Hens, Z.; Gomes, W. P. Electrochemical Impedance Spectroscopy at Semiconductor Electrodes: The Recombination Resistance Revisited. *J. Electroanal. Chem.* **1997**, *437*, 77−83.

(45) Wang, Q.; Moser, J. E.; Grätzel, M. Electrochemical Impedance Spectroscopic Analysis of Dye-Sensitized Solar Cells. *J. Phys. Chem. B* **2005**, *109*, 14945−14953.

(46) Ho, P. K. H.; Kim, J.; Burroughes, J. H.; Becker, H.; Li, S. F. Y.; Brown, T. M.; Cacialli, F.; Friend, R. H. Molecular-Scale Interface Engineering for Polymer Light-Emitting Diodes. *Nature* **2000**, *404*, 481−484.

(47) Guerrero, A.; Montcada, N. F.; Ajuria, J.; Etxebarria, I.; Pacios, R.; Garcia-Belmonte, G.; Palomares, E. Charge Carrier Transport and Contact Selectivity Limit the Operation of PTB7-Based Organic Solar Cells of Varying Active Layer Thickness. *J. Mater. Chem. A* **2013**, *1*, 12345−12354.

(48) Kirchartz, T.; Gong, W.; Hawks, S. A.; Agostinelli, T.; MacKenzie, R. C. I.; Yang, Y.; Nelson, J. Sensitivity of the Mott-Schottky Analysis in Organic Solar Cells. *J. Phys. Chem. C* **2012**, *116*, 7672−7680.

(49) Zonno, I.; Martinez-Otero, A.; Hebig, J. C.; Kirchartz, T. Understanding Mott-Schottky Measurements under Illumination in Organic Bulk Heterojunction Solar Cells. *Phys. Rev. Appl.* **2017**, *7*, 034018.

(50) Almora, O.; Aranda, C.; Mas-Marzá, E.; Garcia-Belmonte, G. On Mott-Schottky Analysis Interpretation of Capacitance Measurements in Organometal Perovskite Solar Cells. *Appl. Phys. Lett.* **2016**, *109*, 173903.

(51) Lang, D. V. Deep-Level Transient Spectroscopy: A New Method to Characterize Traps in Semiconductors. *J. Appl. Phys.* **1974**, *45*, 3023−3032.

(52) Walter, T.; Herberholz, R.; Müller, C.; Schock, H. W. Determination of Defect Distributions from Admittance Measurements and Application to Cu(In,Ga)Se2 Based Heterojunctions. *J. Appl. Phys.* **1996**, *80*, 4411−4420.

(53) Mertens, V.; Parisi, J.; Reineke-Koch, R. Defect Study on the Indium-Gallium Alloy System of Copper Chalcopyrites Performed on Solar Cell Heterostructures. *J. Appl. Phys.* **2007**, *101*, 104507.

(54) Duan, H. S.; Zhou, H.; Chen, Q.; Sun, P.; Luo, S.; Song, T. Bin; Bob, B.; Yang, Y. The Identification and Characterization of Defect States in Hybrid Organic-Inorganic Perovskite Photovoltaics. *Phys. Chem. Chem. Phys.* **2015**, *17*, 112−116.

(55) Cao, Q.; Gunawan, O.; Copel, M.; Reuter, K. B.; Chey, S. J.; Deline, V. R.; Mitzi, D. B. Defects in Cu(In,Ga)Se2chalcopyrite Semiconductors: A Comparative Study of Material Properties, Defect States, and Photovoltaic Performance. *Adv. Energy Mater.* **2011**, *1*, 845−853.

(56) Carr, J. A.; Chaudhary, S. The Identification, Characterization and Mitigation of Defect States in Organic Photovoltaic Devices: A Review and Outlook. *Energy Environ. Sci.* **2013**, *6*, 3414−3438.

(57) Xu, L.; Wang, J.; Hsu, J. W. P. Transport Effects on Capacitance-Frequency Analysis for Defect Characterization in Organic Photovoltaic Devices. *Phys. Rev. Appl.* **2016**, *6*, 064020.

(58) Boix, P. P.; Garcia-Belmonte, G.; Muñecas, U.; Neophytou, M.; Waldauf, C.; Pacios, R. Determination of Gap Defect States in Organic Bulk Heterojunction Solar Cells from Capacitance Measurements. *Appl. Phys. Lett.* **2009**, *95*, 233302.

(59) Ecker, B.; Nolasco, J. C.; Pallarés, J.; Marsal, L. F.; Posdorfer, J.; Parisi, J.; von Hauff, E. Degradation Effects Related to the Hole Transport Layer in Organic Solar Cells. *Adv. Funct. Mater.* **2011**, *21*, 2705−2711.

(60) Igalson, M.; Zabierowski, P. Transient Capacitance Spectroscopy of Defect Levels in CIGS Devices. *Thin Solid Films* **2000**, *361*, 371−377.

(61) Zheng, X.; Chen, B.; Dai, J.; Fang, Y.; Bai, Y.; Lin, Y.; Wei, H.; Zeng, X. C.; Huang, J. Defect Passivation in Hybrid Perovskite Solar Cells Using Quaternary Ammonium Halide Anions and Cations. *Nat. Energy* **2017**, *2*, 17102.

(62) Hegedus, S. S.; Fagen, E. A. Midgap States in A-Si:H and a-SiGe:H p-i-n Solar Cells and Schottky Junctions by Capacitance Techniques. *J. Appl. Phys.* **1992**, *71*, 5941−5951.

(63) Wang, S.; Kaienburg, P.; Klingebiel, B.; Schillings, D.; Kirchartz, T. Understanding Thermal Admittance Spectroscopy in Low-Mobility Semiconductors. *J. Phys. Chem. C* **2018**, *122*, 9795−9803.

(64) Cole, K. S.; Cole, R. H. Dispersion and Absorption in Dielectrics I. Alternating Current Characteristics. *J. Chem. Phys.* **1941**, *9*, 341−351.

(65) Havriliak, S.; Negami, S. A Complex Plane Representation of Dielectric and Mechanical Relaxation Processes in Some Polymers. *Polymer* **1967**, *8*, 161−210.

(66) Kalmykov, Y. P.; Coffey, W. T.; Crothers, D. S. F.; Titov, S. V. Microscopic Models for Dielectric Relaxation in Disordered Systems. *Phys. Rev. E* **2004**, *70*, 11.

(67) Jonscher, A. K. The 'Universal' Dielectric Response - Review Article. *Nature* **1977**, *267*, 673−679.

(68) Jonscher, A. K. Dielectric Relaxation in Solids. *J. Phys. D: Appl. Phys.* **1999**, *32*, R57.

(69) Sami, S.; Haase, P. A. B.; Alessandri, R.; Broer, R.; Havenith, R. W. A. Can the Dielectric Constant of Fullerene Derivatives Be Enhanced by Side-Chain Manipulation? A Predictive First-Principles Computational Study. *J. Phys. Chem. A* **2018**, *122*, 3919−3926.

(70) Bernardo, B.; Cheyns, D.; Verreet, B.; Schaller, R. D.; Rand, B. P.; Giebink, N. C. Delocalization and Dielectric Screening of Charge Transfer States in Organic Photovoltaic Cells. *Nat. Commun.* **2014**, *5*, 3245.

(71) Torabi, S.; Jahani, F.; Van Severen, I.; Kanimozhi, C.; Patil, S.; Havenith, R. W. A.; Chiechi, R. C.; Lutsen, L.; Vanderzande, D. J. M.; Cleij, T. J.; et al. Strategy for Enhancing the Dielectric Constant of Organic Semiconductors Without Sacrificing Charge Carrier Mobility and Solubility. *Adv. Funct. Mater.* **2015**, *25*, 150−157.

(72) Hughes, M. P.; Rosenthal, K. D.; Ran, N. A.; Seifrid, M.; Bazan, G. C.; Nguyen, T. Q. Determining the Dielectric Constants of Organic Photovoltaic Materials Using Impedance Spectroscopy. *Adv. Funct. Mater.* **2018**, *28*, 1801542.

(73) Torabi, S.; Cherry, M.; Duijnstee, E. A.; Le Corre, V. M.; Qiu, L.; Hummelen, J. C.; Palasantzas, G.; Koster, L. J. A. Rough Electrode Creates Excess Capacitance in Thin-Film Capacitors. *ACS Appl. Mater. Interfaces* **2017**, *9*, 27290−27297.

(74) Lin, Q.; Armin, A.; Nagiri, R. C. R.; Burn, P. L.; Meredith, P. Electro-Optics of Perovskite Solar Cells. *Nat. Photonics* **2015**, *9*, 106−112.

(75) Juarez-Perez, E. J.; Sanchez, R. S.; Badia, L.; Garcia-Belmonte, G.; Kang, Y. S.; Mora-Sero, I.; Bisquert, J. Photoinduced Giant Dielectric Constant in Lead Halide Perovskite Solar Cells. *J. Phys. Chem. Lett.* **2014**, *5*, 2390−2394.

(76) Almond, D. P.; Bowen, C. R. An Explanation of the Photoinduced Giant Dielectric Constant of Lead Halide Perovskite Solar Cells. *J. Phys. Chem. Lett.* **2015**, *6*, 1736−1740.

(77) Poglitsch, A.; Weber, D. Dynamic Disorder in Methylammoniumtrihalogenoplumbates (II) Observed by Millimeter-Wave Spectroscopy. *J. Chem. Phys.* **1987**, *87*, 6373−6378.

(78) Onoda-Yamamuro, N.; Matsuo, T.; Suga, H. Dielectric Study of CH3NH3PbX3(X = Cl, Br, I). *J. Phys. Chem. Solids* **1992**, *53*, 935−939.

(79) Green, M. A.; Ho-Baillie, A.; Snaith, H. J. The Emergence of Perovskite Solar Cells. *Nat. Photonics* **2014**, *8*, 506−514.

(80) Guzelturk, B.; Belisle, R. A.; Bruening, K.; Smith, M. D.; Prasanna, R.; Yuan, Y.; Gopalan, V.; Tassone, C. J.; Karunadasa, H. I.; McGehee, M. D.; et al. Terahertz Emission from Hybrid Perovskites Driven by Ultrafast Charge Separation and Strong Electron-Phonon Coupling. *Adv. Mater.* **2018**, *30*, 1704737.

(81) Kesters, J.; Govaerts, S.; Pirotte, G.; Drijkoningen, J.; Brande, N. Van Den; Liu, X.; Fahlman, M.; Mele, B. Van; Lutsen, L.; Vanderzande, D.; et al. High-Permittivity Conjugated Polyelectrolyte Interlayers for High-Performance Bulk Heterojunction Organic Solar Cells. *ACS Appl. Mater. Interfaces* **2016**, *8*, 6309.

(82) Bonn, M.; Miyata, K.; Hendry, E.; Zhu, X. Y. Role of Dielectric Drag in Polaron Mobility in Lead Halide Perovskites. *ACS Energy Lett.* **2017**, *2*, 2555−2562.

(83) Bassler, H. Charge Transport in Disordered Organic Photoconductors - a Monte-Carlo Simulation Study. *Phys. Status Solidi B* **1993**, *175*, 15−56.

(84) Coropceanu, V.; Cornil, J.; da Silva Fihlo, D. A.; Olivier, Y.; Silbey, R.; Bredas, J. L. Charge Transport in Organic Semiconductors. *Chem. Rev.* **2007**, *107*, 926−952.

(85) Mihailetchi, V. D.; Wildeman, J.; Blom, P. W. M. Space-Charge Limited Photocurrent. *Phys. Rev. Lett.* **2005**, *94*, 126602.

(86) Blakesley, J. C.; Castro, F. A.; Kylberg, W.; Dibb, G. F. A.; Arantes, C.; Valaski, R.; Cremona, M.; Kim, J. S.; Kim, J. S. Towards Reliable Charge-Mobility Benchmark Measurements for Organic Semiconductors. *Org. Electron.* **2014**, *15*, 1263−1272.

(87) von Hauff, E.; Dyakonov, V.; Parisi, J. Study of Field Effect Mobility in PCBM Films and P3HT:PCBM Blends. *Sol. Energy Mater. Sol. Cells* **2005**, *87*, 149−156.

(88) von Hauff, E.; Parisi, J.; Dyakonov, V. Investigations of the Effects of Tempering and Composition Dependence on Charge Carrier Field Effect Mobilities in Polymer and Fullerene Films and Blends. *J. Appl. Phys.* **2006**, *100*, 043702.

(89) von Hauff, E.; Johnen, F.; Tunc, A. V.; Govor, L.; Parisi, J. Detailed Investigation of the Conducting Channel in Poly(3-Hexylthiophene) Field Effect Transistors. *J. Appl. Phys.* **2010**, *108*, 063709.

(90) Tanase, C.; Meijer, E. J.; Blom, P. W. M.; de Leeuw, D. M. Unification of the Hole Transport in Polymeric Field-Effect Transistors and Light-Emitting Diodes. *Phys. Rev. Lett.* **2003**, *91*, 216601.

(91) Važgėla, J.; Genevičius, K.; Juška, G. I-CELIV Technique for Investigation of Charge Carriers Transport Properties. *Chem. Phys.* **2016**, *478*, 126−129.

(92) MacKenzie, R. C. I.; Shuttle, C. G.; Chabinyc, M. L.; Nelson, J. Extracting Microscopic Device Parameters from Transient Photocurrent Measurements of P3HT:PCBM Solar Cells. *Adv. Energy Mater.* **2012**, *2*, 662−669.

(93) Kniepert, J.; Schubert, M.; Blakesley, J. C.; Neher, D. Photogeneration and Recombination in P3HT/PCBM Solar Cells

Probed by Time-Delayed Collection Field Experiments. *J. Phys. Chem. Lett.* **2011**, *2*, 700−705.

(94) Kniepert, J.; Neher, D. Effect of the RC Time on Photocurrent Transients and Determination of Charge Carrier Mobilities. *J. Appl. Phys.* **2017**, *122*, 195501.

(95) Xiang, J.; Cai, L.; Yao, Y. Q.; Ding, B. F.; Alameh, K.; Song, Q. L. A Simple Method to Experimentally Determine the Accurate RC-Constant in Nanosecond Timescale Transient Photocurrent Measurements on Organic Solar Cells. *RSC Adv.* **2015**, *5*, 103403−103409.

(96) Martens, H. C. F.; Huiberts, J. N.; Blom, P. W. M. Simultaneous Measurement of Electron and Hole Mobilities in Polymer Light-Emitting Diodes. *Appl. Phys. Lett.* **2000**, *77*, 1852.

(97) Murgatroyd, P. N. Theory of Space-Charge-Limited Current Enhanced by Frenkel Effect. *J. Phys. D: Appl. Phys.* **1970**, *3*, 151.

(98) Martens, H. C. F.; Brom, H. B.; Blom, P. W. M. Frequency-Dependent Electrical Response of Holes in Poly(p-Phenylene Vinylene). *Phys. Rev. B: Condens. Matter Mater. Phys.* **1999**, *60*, R8489−R8492.

(99) Tsang, S. W.; So, S. K.; Xu, J. B. Application of Admittance Spectroscopy to Evaluate Carrier Mobility in Organic Charge Transport Materials. *J. Appl. Phys.* **2006**, *99*, 013706.

(100) Berleb, S.; Brütting, W. Dispersive Electron Transport in Tris(8-Hydroxyquinoline) Aluminum ([Formula Presented]) Probed by Impedance Spectroscopy. *Phys. Rev. Lett.* **2002**, *89*, 286601.

(101) Tripathi, D. C.; Tripathi, A. K.; Mohapatra, Y. N. Mobility Determination Using Frequency Dependence of Imaginary Part of Impedance (Im Z) for Organic and Polymeric Thin Films. *Appl. Phys. Lett.* **2011**, *98*, 033304.

(102) Gommans, H. H. P.; Kemerink, M.; Andersson, G. G.; Pijper, R. M. T. Charge Transport and Trapping in Cs-Doped Poly(Dialkoxy-p-Phenylene Vinylene) Light-Emitting Diodes. *Phys. Rev. B: Condens. Matter Mater. Phys.* **2004**, *69*, 155216.

(103) Okachi, T.; Nagase, T.; Kobayashi, T.; Naito, H. Determination of Charge-Carrier Mobility in Organic Light-Emitting Diodes by Impedance Spectroscopy in Presence of Localized States. *Jpn. J. Appl. Phys.* **2008**, *47*, 8965−8972.

(104) Monroe, D. Hopping in Exponential. *Phys. Rev. Lett.* **1985**, *54*, 146−149.

(105) Baranovskii, S. D. Theoretical Description of Charge Transport in Disordered Organic Semiconductors. *Phys. Status Solidi B* **2014**, *251*, 487−525.

(106) Bisquert, J.; Bertoluzzi, L.; Mora-Sero, I.; Garcia-Belmonte, G. *J. Phys. Chem. C* **2014**, *118*, 18983−18991.